ETH
Eidgenössische Technische Hochschule Zürich
Swiss Federal Institute of Technology Zurich

Masterthesis

Towards high fidelity two-qubit gates with superconducting qubits

Author:
Johannes Heinsoo

Supervisor:
Yves Salathé
Prof. Andreas Wallraff

spring 2014

Contents

1 Introduction **3**

1.1 Motivation . . . 3
1.2 Short overview of the development of the field . . . 4
1.3 Realization of the qubit . . . 6
1.4 Two-qubit operations . . . 8
1.5 Numeric simulations . . . 10
1.6 Experiment setup . . . 12

2 Shape optimization of flux pulses **16**

2.1 Interaction length and amplitude . . . 16
2.2 Flux screening . . . 21
2.3 Flux pulse ringing . . . 23
2.4 Dynamic phases . . . 25
2.5 Conditional phase . . . 26
2.6 Discussion and outlook . . . 30

3 Process tomography **32**

3.1 Two-qubit readout and state tomography . . . 32
3.2 Optimizing the readout parameters . . . 34
3.3 Input-output map & error syndromes . . . 37
3.4 Pauli transfer matrix . . . 41
3.5 Process matrix representation . . . 42
3.6 Phase degree of freedom . . . 45
3.7 Choi matrix and qubit decay . . . 47

Summary and acknowledgements **51**

A Notation **53**

B Data set details **56**

References **57**

Abstract

The fundamental element of a quantum computation is a single quantum operation of quantum bits or qubits. At this point most of the interesting quantum information experiments are done with superconducting transmon type qubits coupled to microwave cavities acting as quantum information bus. In this architecture the qubit states are manipulated with short DC and microwave pulses. While accurate single-qubit operations are routine there is room for improvements regarding multi-qubit quantum logic gates. The present thesis gives an overview of calibration routines of two-qubit gates and compares the different representations of quantum processes relevant for experimentalists. The described tools enabled two qubit operation fidelities above 81 % and several suggestions will be made on how to further improve the calibration routines in order to resolve the remaining fidelity.

1 Introduction

This chapter will give a short overview of background and methods for the discussion following. Before providing an summery of the theoretical and experimental approach to quantum information experiments, that have been pursued in the present thesis, I will provide a short motivation for the field. I will also provide a summary of history of the relevant achievements of the last few decades, which have enabled the late rapid development of the field we have witnessed in last 10 years.
In Chapter 2 I will cover the experimental methods for characterising and calibrating the flux pulses used for two-qubit gates. The description of the state and process tomography which allows the full characterization of a quantum process, is provided in Chapter 3. Appendix A provides the reference for the notation used throughout the thesis and Appendix B covers the details of presented data sets.

1.1 Motivation

By today the increasing computational capabilities are widely exploited in all fields of science, medicine, technology and entertainment. Some of the computational problems however have remained out of reach because they appear to be particularly hard. In information theory a problem is considered more difficult than another, if the amount of needed resources to solve the problem, like time or memory capacity, grows faster with the size of the problem. Some of the problems which are hard for classical computers have turned out to scale considerably better for computing machines able to make use of quatum phenomena, like quantum superposition, entanglement and tunnelling. The effort of building a quantum computer is not justified for small problems, if the a classical computer can solve it even if inefficiently. But there are cases where the problem only becomes interesting for a size, where amount of needed resources for classical computers reaches cosmic scales. For example only a full description of 300 qubits in a pure state requires $2^{300} \approx 2 \times 10^{90}$ complex numbers which is larger than a number of atoms in observable universe – if size matters, then Hilbert space matters a lot.
Probably the best known example of problems that scale better in quantum implementations is the integer number factorization problem, which is the core element of modern cryptographic methods like the widely used RSA [Nielsen 00, App. A]. The problem turns out to be solvable with polynomial complexity using Shors algorithm [Nielsen 00, Ch. 5]. Actually there is a wide class of problems hard to solve in classical systems called NP-complete, which includes many important optimisation problems also shown to be easier to solve on a quan-

tum computer [Santoro 06]. Maybe the most important application for science would be the ability to simulate other quantum systems like the Heisenberg spin chain, which is attempted in our lab [Las Heras 14]. The quantum simulations are hard for classical computers due to the already mentioned scaling of the state space. In addition to the direct applications, the effort put into the development of quantum systems for information technology helps to understand the quantum aspects of the nature in general and thus is of value in fundamental science.

A quantum computer able to carry out an arbitrary quantum algorithm is called *universal*. To succeed in building it, one needs to implement a *universal set of quantum gates*. It can be shown that it is enough, to have a single multi-qubit operation capable of creating entanglement, a non-classical manifestation of multi-qubit correlation, in addition to a full control of a single qubit [Nielsen 00, Ch. 4]. Having ability to make longer sequences of quantum gates enables investigation of more interesting and important quantum algorithms. Due to errors piling up, the fidelity of any single gates is increasingly important in case of long algorithms.

The goal of the present thesis is to improve the fidelity of our two-qubit gates. This requires improved toolset and its documentation of our standard methods for characterising, calibrating and describing the operations. In order to scale up the implementation towards more complex set-ups, the calibration methods have to be as automatized, modular and robust as possible to run without human supervision. The possible improvements can be seen only when having the full information of the achieved quantum operation. For this a set of measurements is needed, referred to as quantum process tomography. It would be impossible to draw useful conclusions from the gained information without proper way of visualizing it and therefore we will discuss different representations of the quantum process. Thus the different aspects of the present thesis are strongly connected and are all essential for achieving the goal we set.

1.2 Short overview of the development of the field

The first applications of laws of quantum physics for information technology were proposed by Stephen Wiesner in the early 60s [Nielsen 00, Ch. 1]. In addition to principles of quantum cryptography and superdense coding he proposed non-forgeable quantum currency [Wiesner 83].

Photonics was the first field to give access to physical implementation of quantum computing concepts [Nielsen 00, Ch. 7.4]. This was because photons interact weakly to the environment, availability of strong sources of photons in non-classical states and straightforward mapping

of polarisation states from Poincaré's sphere to the Bloch sphere describing the qubit state. One of the important achievements of photonics regarding quantum information was the observation of space-time separated qubit entanglement [Aspect 82]. The weak photon-photon interaction however has prevented the up-scaling of optical implementations.

Another early implementation of a qubit was a spin state of a nucleus in an external magnetic field [Nielsen 00, Ch. 7.7]. The tools of nuclear magnetic resonance were well developed due to a variety of other applications and the qubit-qubit interaction are naturally provided by electron intermediated spin couplings in a single molecule. This enabled first implementations of quantum algorithms [Chuang 98]. The big drawbacks of NMR quantum computing are the decrease of qubit coherence with the size of the molecule (number of qubits) [Gershenfeld 97], the thermal population in room temperature experiments and the lack of control over qubit-qubit coupling strength. Thus the approach is probably not scalable [Warren 97] nor suitable for generic quantum computation [Menicucci 02].

In addition to the mentioned optical photonics and NMR quantum computation several other physical implementations have been developed all featuring different conveniences as well as challenges. Among trapped ions [Haffner 08], semiconductor quantum dots [Hanson 08] and NV-centers of diamonds [Childress 13], supperconducting circuits have went through a rapid development in the last ten years and have proven to be one of the most promising approaches [Clarke 08]. They can be considered to consist of artificial atoms in microwave cavities which can be implemented on a single chip. The properties of the superconducting qubits, which are analogues of atoms in the well studied field of cavity quantum electrodymics (QED) [Cohen-Tannoudji 89, Loudon 00], can be designed in a wide range of parameters enabling a whole new subfield of circuit QED [Blais 07].

The qubits are implemented as LC oscillators with some non-linearity. Depending on the design parameters the state quantization carries a different physical meaning which leads to classification into charge, flux and phase qubits. The charge qubit, which is also referred to as *Cooper pair box* (CPB) was first studied in 1987 by Büttiker [Büttiker 87] and its different breeds have remained the most used ones in the modern experiments. The coherent controll of the qubit state was first achieaved in 1999 [Nakamura 99] followed by strong coupling to a coplanar microwave resonator in 2004 [Wallraff 04]. After this qubit-qubit coupling [Steffen 06], multi-qubit state tomography [Filipp 09], error-correction [Reed 12], deterministic teleportation of a quantum state [Steffen 13a] and a 5-qubit GHZ state [Barends 14] has been demonstrated. The limiting factors remain to be signal detection fidelity and qubit lifetime.

1.3 Realization of the qubit

The transmon qubit used in the present experiments, consists of two capacitively coupled superconducting islands connected by Josephson junctions. The junction consists of an oxide layer between two superconducting leads acting as a tunnel barrier for Cooper pairs. In charge representations the Hamiltonian is [Bouchiat 98]

$$\hat{H}(n_g) = \sum_{N=-\infty}^{\infty} \left[4E_C \left(N - N_g\right)^2 |N\rangle \langle N| - \frac{E_J}{2} \left(|N\rangle \langle N+1| + |N+1\rangle \langle N| \right) \right] \tag{1.1}$$

where N stands for the difference in the number of the cooper pairs on two islands, N_g is the external DC bias in units of cooper pair charges, $E_C = (2e)^2/2C_\Sigma$ is the Coulomb energy corresponding to the total capacitance C_Σ between the islands and E_J is the Josephson energy of the junction. The first part of the Hamiltonian provides the harmonic potential and the kinetic term in the Hamiltonian mixes the Cooper pair number states.

Having two junctions in a loop instead of one forms a SQUID (Superconducting QUantum Interference Device) which allows us to use a magnetic field to tune $E_J(\Phi)$ [Tinkham 96, Ch. 6.4.1]. The Hamiltonian 1.1 can be exactly solved in phase representation [Cottet 02, Koch 07] and eigenenergies are given in terms of the Mathieu characteristic function $\mathcal{M}_A(r, q)$ as[1]

$$E_{ik} = E_{C_i} \mathcal{M}_A \left[k + \frac{1}{2} + (-1)^k \left(\left| \mathrm{mod}(1 + 2N_{g_i}, 2) - 1 \right| - \frac{1}{2} \right), -2 \left| \cos \theta_i \right| \frac{E_{Jmax_i}}{E_{C_i}} \right] \tag{1.2}$$

with $\theta = \Phi/\Phi_0$ being the external magnetic field in units of the flux quantum $\Phi_0 = \hbar/(2e)$ and k and i being the index of the energy level and qubit. The first two transition energies are shown in Figure 1. The interpretation is provided with the help of Hamiltonian 1.1. In the case where E_J and E_C are in same order of magnitude, the device is called *Cooper Pair Box* (CPB). Its eigenstates more or less correspond to the number of Cooper pairs in the exited state but due to the kinetic part of Hamiltonian 1.1 the states couple and show an anti-crossing. It is also clear, that E_J is the coupling strength of the charge states lifting the degeneracy and introducing the splitting. In the case of *transmon* qubits (*transmission-line shunted plasma oscillation* qubit), it holds that $E_J \gg E_C$ and $\hat{N}$ stops from being a good quantum number, as the Cooper pair number states will always be hybridized.

In general there are two knobs for tuning the transition frequency of the qubit: the charge bias and external magnetic field. In the case of transmon qubits the sensitivity to gate charge

[1] The expression in the first argument sorts the solutions and the exact form might depend on the conventions used. The form given here was used with the *Wolfram Mathematica 9* function `MathieuCharacteristicA`. See the discussion in [Koch 07, App. B].

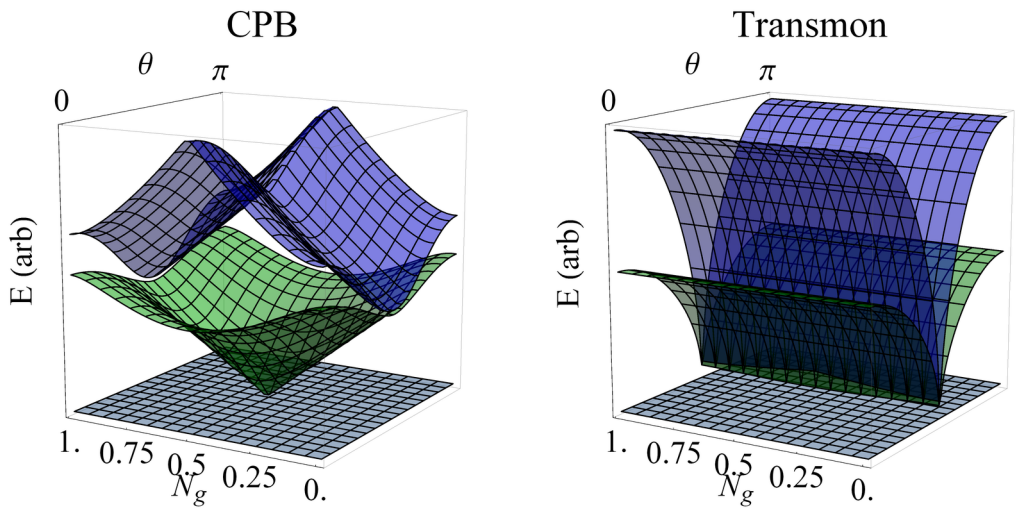

Figure 1: The first two transistion energies of a Cooper Pair Box (CPB) where $E_C = E_J$ and a transmon qubit with $E_J = 100E_C$. In case of the CPB energy varies as function of both, the dimensionless DC bias N_g and dimensionless external magnetic field θ. In case of the transmon qubit the charge sensitivity is strongly decreased. The CPB box is first order insensitive to N_g only in the "sweet spots" where $N_g \bmod 1/2 = 0$.

is suppressed. This reduces the qubit dephasing rate $1/T_2$, which is limited by charge noise in the usual case of the CPB. In addition the large capacitor plains act as an antenna with increased dipole moment for coupling the qubit with other circuit elements. The remaining flux sensitivity is used to tune qubits into resonance with each other for two-qubit gates which will be described in more detail later.

To achieve single-qubit operations the transitions from the ground state g to the first exited state e are driven with short microwave pulses [Baur 12, Ch. 5]. The only downside of the transmon type of qubit is the reduced anharmonicity. This means, that the transition frequencies to the first exited state $\nu_{g\to e}$ and from the first to the second exited state $\nu_{e\to f}$ become similar. This in turn sets a limit on how short the pulses can be, such that they could address a single transition. This problem is somewhat suppressed using special pulse envelopes with a method called *derivative removal by adiabatic gate* (DRAG) [Motzoi 09, Gambetta 11] or more complex *Weak AnHarmonicity With Average Hamiltonian* (Wah-Wah) [Schutjens 13, Vesterinen 14].

1.4 Two-qubit operations

If the qubit i with frequency ω_i has a detuning $\Delta_i = \omega_i - \omega_r$ from the resonator which is large compared to the coupling rate g_i, energy conservation prevents population exchange between the qubit and the resonator. In this so called dispersive regime the Jaynes-Cummings Hamiltonian, describing the two qubits in the cavity, has the form [Blais 07]

$$H_{2q} \approx \hbar\omega_r a^\dagger a + \hbar \sum_{i=1,2} \frac{\tilde{\omega}_i}{2}\sigma_i^z + \hbar \frac{g_1 g_2 \left(\Delta_1 + \Delta_2\right)}{2\Delta_1\Delta_2} \left(\sigma_1^+\sigma_2^- + \sigma_1^-\sigma_2^+\right) \tag{1.3}$$

up to second order in small parameters g_i/Δ_i. The first term of the Hamiltonian represents the energy of photons in the resonator where $a^\dagger$ and a are corresponding creation and annihilation operators. The second term gives the energy of the qubit state with $\tilde{\omega}_i = \omega_i + \chi_i$ being the Lamb shifted qubit frequency [Fragner 08] and χ_i being the magnitude of the corresponding dispersive shift[2]. Here we are most interested in the last term of Hamiltonian 1.3, which is the exchange term with $\sigma_i^+ = |e\rangle\langle g|$ and $\sigma_i^- = |g\rangle\langle e|$ being the rising and lowering operators of qubit i. Such interaction is also called *J-coupling* [Nielsen 00, Ch. 7.7.2] with qubit-qubit coupling strength $J = g_1 g_2 \left(1/\Delta_1 + 1/\Delta_2\right)/2$. Although the resonator is not exchanging any populations with the qubits it provides a channel for photons of virtual state. Thus the resonator acts as a quantum bus coupling together distant qubits [Blais 04, Majer 07].
The $|gg\rangle$ and $|ee\rangle$ states are always eigenstates of the full Hamiltonian given by Equation 1.3, but the states in the one-excitation manifold are mixed by the J-coupling to symmetric and antisymmetric eigenstates [Filipp 11]

$$|\psi_s\rangle = \sin(\theta_m)\,|eg\rangle + \cos(\theta_m)\,|ge\rangle\,, \tag{1.4a}$$

$$|\psi_a\rangle = \cos(\theta_m)\,|eg\rangle - \sin(\theta_m)\,|ge\rangle\,, \tag{1.4b}$$

with θ_m being the mixing angle given by

$$\cos(2\theta_m) = -\delta_q/\sqrt{4J^2 + \delta_q^2} \tag{1.5a}$$

or

$$\sin(2\theta_m) = 2J/\sqrt{4J^2 + \delta_q^2} \tag{1.5b}$$

which depend on the qubit-qubit detuning $\delta_q = \delta_1 - \delta_2$. By tuning the qubits from the interaction position $\delta_q = 0$ to the parking position limit $\delta_q \gg J$, effectively the interqubit in-

[2]For discussion regarding g and χ for transmon qubits refer to [Koch 07, Ch. 3] and [Filipp 11, Ch. 3]. AC Stark shift terms of the form $a^\dagger a\chi\sigma_z$ have been dropped as we are interested in the case where the resonator photon number is low [Blais 07, Sec. III].

teraction is switched off[3] and the eigenstates $|\psi_s\rangle$ and $|\psi_a\rangle$ asymptotically go to $|ge\rangle$ and $|eg\rangle$. In the rotating reference frame (RRF) of the qubits the exchange term of Hamiltonian given by Equation 1.3 provides a time evolution

$$U_{gg}(t) = e^{-it/\hbar H_{int}} = e^{-itJ\left(\sigma_1^+\sigma_2^- + \sigma_1^-\sigma_2^+\right)} = \\ = \begin{pmatrix} 1 & 0 & 0 & 0 \\ 0 & \cos(Jt) & -i\sin(Jt) & 0 \\ 0 & -i\sin(Jt) & \cos(Jt) & 0 \\ 0 & 0 & 0 & 1 \end{pmatrix}. \tag{1.6}$$

For the waiting time $t_{i\text{-SWAP}} = -\pi/(2J)$ this interaction gives us the i-SWAP gate.
Having arbitrary single-qubit operations and the i-SWAP gate we already have a universal set of quantum gates [Brylinski 02, Bremner 02] but to implement a c-NOT (c for *controlled*) one needs two i-SWAP gates [Schuch 03]. By using an evolution through non-computational states it is possible to directly implement a c-PHASE gate [Strauch 03] which can be turned into the c-NOT with single qubit operations.
The non-computational state most easy to access, is the f-level of one of the qubits. The relevant interaction Hamiltonian reads

$$\hat{H}_{eg} = \hbar J_{eg}\left[|fg\rangle\langle ee| + h.c.\right] \tag{1.7}$$

with $h.c.$ standing for the hermitian conjugate of the first term and sub-indexes k and l in $\hat{H}_{kl}$ and J_{kl} standing for qubit states without the extra excitation they exchange in the interaction (in this notation J used before corresponds to J_{gg}). This gives a time evolution of

$$U_{eg}(t) \quad = e^{-it/\hbar H_{eg}} = e^{-itJ\sqrt{2}(|fg\rangle\langle ee| + h.c.)}, \tag{1.8}$$

$$P^\dagger\, U_{eg}(t)\, P = \begin{pmatrix} 1 & 0 & 0 & 0 \\ 0 & 1 & 0 & 0 \\ 0 & 0 & 1 & 0 \\ 0 & 0 & 0 & \cos(J_{eg}t) \end{pmatrix} \tag{1.9}$$

with P projecting from the two 3-level systems, referred to as qutrits, down to the two-qubit space. Note, that the evolution in the subspace is not trace preserving for arbitrary t as the population is oscillating to a state outside of the logical qubit computational bases. However

[3] Another way to see this is by staying in the rotating reference frame of individual qubits and when qubits are far detuned the rapidly oscillating coupling term will average out which is interpreted as a consequence of energy conservation [Blais 07].

for the waiting time of $t_{\text{c-PHASE}} = \pi/(J_{eg})$ the J_{eg} coupling gives us a c-PHASE gate. If one wraps the $U_{J_{eg}}$ with single qubit $Y(\frac{\pi}{2})$ gates the resulting propagator is

$$Y(\tfrac{\pi}{2})\, P^{\dagger}\, U_{eg}(t)\, P\, Y(\tfrac{\pi}{2})^{\dagger} = \begin{pmatrix} 1 & 0 & 0 & 0 \\ 0 & 1 & 0 & 0 \\ 0 & 0 & \cos(Jt/\sqrt{2})^2 & \sin(Jt/\sqrt{2})^2 \\ 0 & 0 & \sin(Jt/\sqrt{2})^2 & \cos(Jt/\sqrt{2})^2 \end{pmatrix}. \tag{1.10}$$

which gives c-NOT operations for $t_{\text{c-NOT}} = t_{i\text{-SWAP}} = \pi/(J_{eg})$.
It is also possible to do the two-qubit operations by driving sidebands [Wallraff 07], but such schemes are slower than flux pulse based schemes.

1.5 Numeric simulations

As some measurements take a lot of time, it is useful to study the ideas with numeric simulations. Here and later in this thesis theoretical data presented is derived from the two qutrit J-coupling Hamiltonian of the form

$$H_{sim} = H_{bare} + H_{int}. \tag{1.11}$$

For the interaction term

$$\hat{H}_{int}/\hbar = J\left[\left(|0\rangle\langle 1|_A + \sqrt{2}|1\rangle\langle 2|_A\right) \otimes \left(|1\rangle\langle 0|_B + \sqrt{2}|2\rangle\langle 1|_B\right) + h.c.\right] \tag{1.12}$$

we assume the qubit detuning Δ to be much larger than the qubit anharmonicity, which allowed the relation $J_{eg} = \sqrt{2}J_{gg}$ [Baur 12, Ch. 6]. The resonator term has been completely dropped as we assume the resonator to be in the ground state. The term H_{bare} describes the system made out of bare qubits and is the part, which is tuned by external field as

$$\begin{aligned} H_{bare} &= \sum_{i,k} |k\rangle\langle k|_i \hbar\tilde{\omega}_{ik} = \\ &= \sum_{i,k} |k\rangle\langle k|_i \left(E_{ik}(\theta_i) - E_{ig}(\theta_i)\right). \end{aligned} \tag{1.13}$$

Here $i \in \{A, B\}$ is the index of the qubit and $k \in \{g, e, f\}$ is the index of the qubit state. The dispersively shifted qubit frequency $\tilde{\omega}$ can be taken to correspond to $E_k - E_g$ defined in equation 1.2 as the parameters for the latter are taken from the spectroscopy, which already takes χ_i into account. Both χ and g are taken to be constant in the studied range which does introduce a small quantitative error, but it simplifies the symbolic form of the simulations considerably[4].

[4] See also comments on Equation 1.3.

Relevant qubit transition frequencies of H_{sim} are shown in Figure 2 as a function of qubit A dimensionless magnetic flux or *flux angle* θ_A. The parameter for numeric evaluation here and later are shown in Table 1. Qubits A and B correspond on the actual chip shown in Figure 4 to qubit $A = 2$ and qubit $B = 1$. Throughout the thesis the experiments and simulations are shown for the same qubits.

It is worth pointing out, that even at the parking frequencies of the qubits the qubit-qubit J-coupling is not completely switched off and the transition energies are little shifted from the $\tilde{\omega}_i$[5]. To avoid the qubit state from evolving in the parking position, where we intend to do nothing, we stay in the RRF with frequency $\overline{\nu}$ of the so called *dressed* state of the qubit[6]. For the two qubit operations qubit A will be shortly tuned into resonance with B as indicated in Figure 2 with vertical lines. The separation of $\theta_{i\text{-SWAP}}$ and $\theta_{\text{c-PHASE}}$, which is due to qubit anharmonicities, allows to implement time evolution 1.6 or 1.10 independently. At the anticrossing the bare qubit states have the time evolution in relation to uncoupled bare states. During the gate the later is used for the RRF because if the coupling would not be present, the gate should not alter the qubit state. The corresponding propagators in the RRF of the dressed and bare states are defined as

$$U_{bare} = U_{sim}\ (Z(t\tilde{\omega}_A) \otimes Z(t\tilde{\omega}_B)) \tag{1.14a}$$

$$U_{dressed} = U_{sim}\ (Z(t\overline{\omega}_A) \otimes Z(t\overline{\omega}_B)) \tag{1.14b}$$

where $U_{sim} = P^\dagger \exp(-it/\hbar H_{sim})P$ is a function of t and θ as is H_{sim} defined in Equation 1.11. Later on, both RRFs will be used and the difference has to kept in mind.

To prevent the leaf-counts of symbolic expressions from growing too high, a second-order polynomial approximation is used instead of exact Mathieu functions around qubit parking

[5] Actually even what was called the *bare* qubit state is finitely hybridized with the resonator.

[6] This point is also discussed in depth [Ghosh 13, Ch. III-c].

	Qb A	Qb B	
E_C/h	0.303 GHz	0.297 GHz	from [Steffen 13a]
$\nu_{maximum}$	7.373 GHz	6.273 GHz	
$\nu_{parking}$	6.5898 GHz	5.8874 GHz	
$J_{00}/2\pi$	14.9 Mhz		measured recently

Table 1: Parameters used in the simulation. First group of parameters are taken from [Steffen 13a] which also describes the sample used in the experiments for the thesis. Second group of parameters is directly observed.

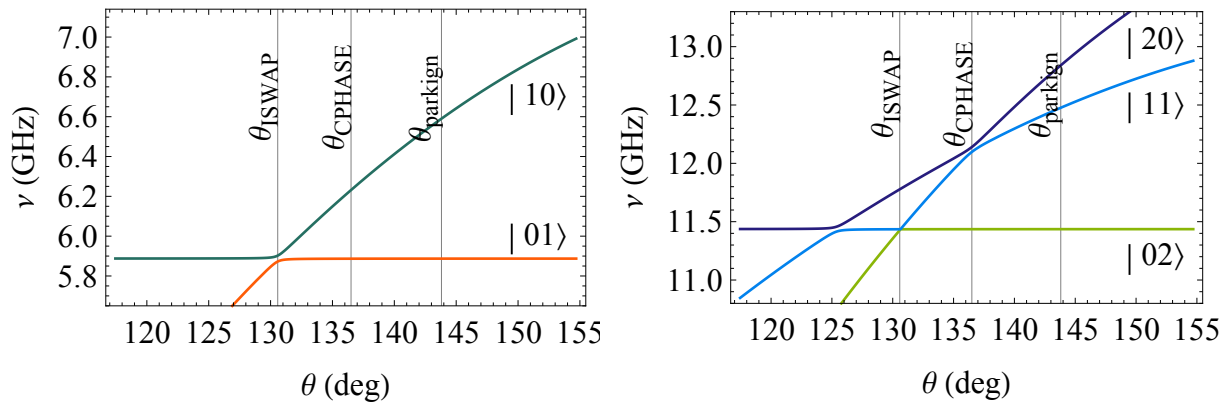

Figure 2: Energy dependence of two qubit states on the flux bias of qubit A. The flux bias used for c-PHASE, i-SWAP and qubit parking are marked with a vertical lines. When the energies of two states are tuned to resonance, they are shifted by J_{kl}/π due to qubit-qubit coupling. The splitting is smaller for the second order process at the anti-crossing of $|02\rangle$ and $|20\rangle$.

flux angle. This is both easier to evaluate symbolically and is more precise than the cosine approximation often used. The comparison is shown in Figure 3. One could also just use the frequency $\tilde{\omega}$ as the parameter instead of θ, but the relative qubit anharmonicity is not constant over θ and we use the polynomials to describe the dynamics with higher states more accurately.

1.6 Experiment setup

The experiments in this thesis were carried out with the sample for the quantum state teleportation experiment [Steffen 13a] and is shown in Figure 4. It has four transmon qubits capacitively coupled to coplanar transmission line resonators at the anti nodes of the standing wave of the chosen mode.

The ends of two of the resonators are coupled to input and output ports for transmission measurements. As the qubits are strongly coupled to the resonators they induce state dependent resonator frequency shifts even when far detuned from the resonator[7]. The readout method is called *dispersive readout* [Wallraff 04]. As the transmitted signal has a strength on the order of less than 10 photons (to avoid qubit driving), it is first amplified using a quantum limited Josephson Parametric Dimer (JPD) [Eichler 14] and then with other cold and warm amplifiers before down-conversion and digital homodyne measurement using custom firmware

[7]Shown using the dispersive regime of the generalised Jaynes-Cummings model [Blais 04].

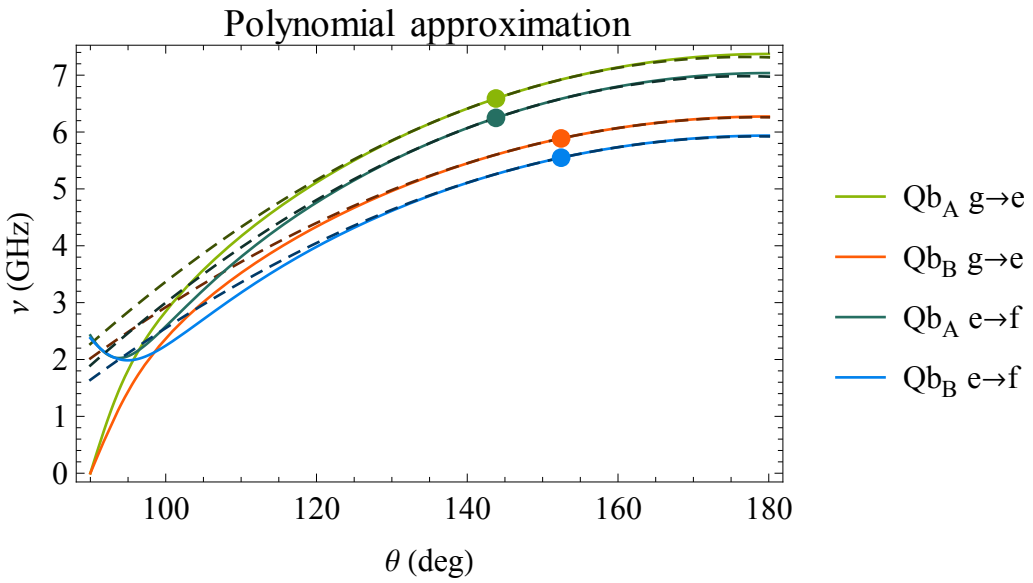

Figure 3: Transition frequencies $\overline{\nu}$ from ground to first exited and from first exited to second exited are shown as a function of dimensionless flux angle θ. The exact values are shown with solid lines and second order polynomial approximations are denoted with dashed lines. The series expansions is done at the qubit parking positions indicated with dots.

on FPGA [Lang 13]. In case of averaged readout, the signal is averaged 2×10^3 to 100×10^3 times depending on the nature of the measurement. The integrated difference of calibration and measurement time traces maps the two-qubit population into a single number here referred to as *M-value*. The scaled and normalized mapping is described by a measurement operator

$$M = \begin{pmatrix} 0 & 0 & 0 & 0 \\ 0 & m_{eg} & 0 & 0 \\ 0 & 0 & m_{ge} & 0 \\ 0 & 0 & 0 & 1 \end{pmatrix} \tag{1.15}$$

where positive real numbers m_{eg} and m_{ge} in the range $[0, 1]$ are related to qubit state dependent changes in resonator transmission [Filipp 09]. The analysis and measurement operator are discussed in more detail in Section 3.1.

In addition to the qubits and resonators there are voltage bias and flux lines for each qubit on the sample. As we use transmon qubits, we don't need to DC bias the qubits, but the lines are used to drive the qubit transitions with microwave (MW) pulses from 4 to 9 GHz depending on the qubit parking position. The parking position is set with 3 off-chip coils providing the ability to park relevant qubits independently at the specified frequency. The

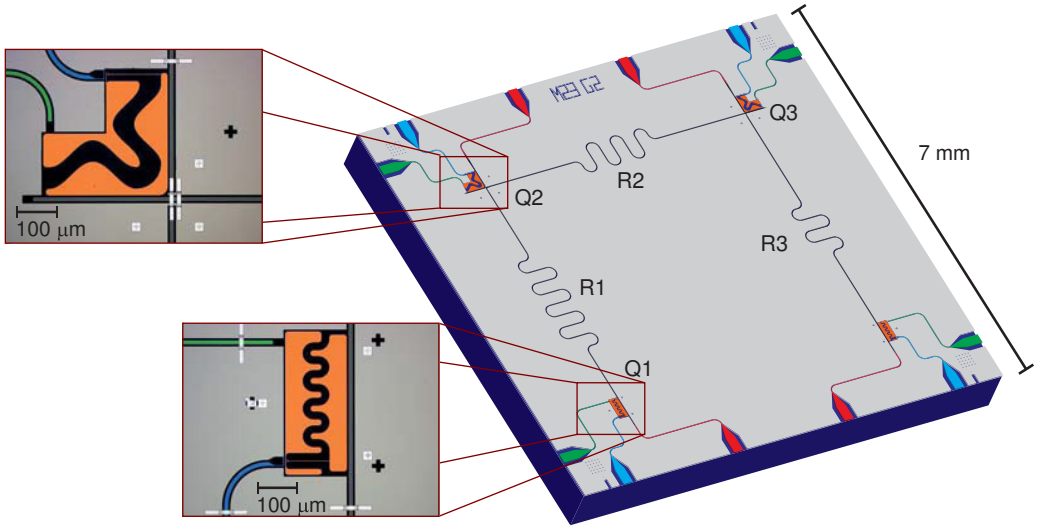

Figure 4: Rendered image of the sample used for the experiments described in this thesis. There are four qubits with voltage bias lines (green) and magnetic flux lines (blue). Qubits are connected with three resonators, out of which R1 and R3 are connected to input and output ports (red). Sample fabrication, characteristics and image courtesy [Steffen 13a].

qubit flux lines are used to detune the qubits from their parking position to achieve two-qubit gates using nanosecond scale DC pulses described in more detail later.

To carry out algorithms composed of qubit manipulation pulses, when the typical lifetime of the qubit is few μs, the operations have to be fast. A typical single qubit pulse has a waist width of 3 ns. To produce arbitrary MW waveforms in this time scale, a 1.2 GS/s arbitrary waveform generator (AWG) is used. The patterns are compiled for both signal quadratures on the measurement PC with intermediate frequency $\nu_{IF} =$ 150 MHz and loaded into the AWG. The output of a channel pair is then directed to an IQ-mixer to be upconverted for qubit (qb) manipulation with local oscillator frequency $\nu_{LO} = \nu_{qb} + \nu_{IF}$ from phase locked MW generator. Having not only the amplitude, but also the phase modulation allows us to drive the qubit around both x and y axes of the Bloch sphere [Baur 12, Ch. 5]. The rotations around z axes, the PHASEgate can be done by change in computational bases (phase of AWG pulses can be arbitrary) or with fast flux pulses, which would detune the qubit for short period from its computational bases RRF. The flux pulses are also produced with the same AWG-s and thus limited to 0.8 ns time resolution.

Care has to be taken to suppress different kinds of environment noise. Around the sample holder are magnetic fields shields. To prevent thermal excitation of MW range qubits is cooled down by ^{3}He/ ^{4}He dilution refrigerator with usual base plate temperature of 20 to

30 mK. Not only the mechanical components have to be cold, but also the signals reaching the sample. This is done by attenuating the incoming signals at each temperature stage. At each stage this suppresses the temperature radiation from the previous stage with the cost of adding the temperature field of the thermalized attenuator itself.
More detailed description of the setup of circuit QED experiments is provided in [Steffen 13b, Ch. 4] and [Baur 12, Ch. 4].

2 Shape optimization of flux pulses

Different experiments with long sequences of multi-qubit operations have already been carried out [Córcoles 13, Barends 14]. In the case where the gate is used multiple times in a long sequence it is increasingly important to achieve highest possible gate fidelity.
Our goal is to achieve such calibrated operation blocks, which could be concatenated into a long algorithm after independent calibration of single blocks. This means the gate should in no way depend on the history as otherwise calibration of all combinations might be needed, which would remove the scaling advantage the quantum algorithms possess. Here I describe the calibration methods implemented as automatic routines in the *QubitCalib* software suite developed in our lab [Menke 13, Landig 13, Heinsoo 13]. Some effects we discuss could be avoided with different sample design (like the screening current described in Section 2.2) or better control hardware (flux pulse ringing in Section 2.3), but some are fundamental to this kind of system.
The following discussion focuses on the calibration of the i-SWAP gate needed for planned quantum simulation experiments [Las Heras 14], but the flux pulse model built throughout the discussion holds for other two qubit operation blocks including the two-qubit identity gate, which also needs calibration as it too suffers from the residual coupling discussed in Section 2.5. Similar calibration methods for c-PHASE gate are discussed in [Baur 12] and in [Heinsoo 13].

2.1 Interaction length and amplitude

As described in Section 1.4 there are two knobs to be tuned to achieve i-SWAP operations with dynamics of our system: the amplitude of the flux pulse, which would tune the qubit A from ν_A to $\nu_{i\text{-SWAP}}$, the resonance with qubit B, and the length of the flux pulse which corresponds to the exact J-coupling strength of the states. The most straight forward way to evaluate the correctness of the parameters is to measure the expected exchange of population between two qubits on resonance.
To measure the exchange of qubit population we first take qubit A to the exited state using a π rotation around the X axes of the Bloch sphere by a short on-resonance MW pulse. Then we apply a square flux pulse through the local flux line of qubit A. If the flux pulse is close to the i-SWAP operation, qubit B should now be exited. One more π-pulse is applied on qubit A to increase the visibility in the dispersive readout[8]. The used pulse scheme is

[8]The $|gg\rangle$ and $|ee\rangle$ states are easier to separate than $|ge\rangle$ and $|eg\rangle$. The two-qubit measurement scheme is discussed in more detail in Section 3.1.

illustrated in Figure 5b. If the interaction length was too long or too short, or the exchange of population was not complete due to wrong amplitude of the flux pulse, the $|gg\rangle$ state is found instead of $|ee\rangle$ and we get a 2D landscape shown in Figure 5a. Note that the outcome would be the same, if the π-pulses would be done on the other qubit due to the symmetry of the gate.

The optimal flux pulse length and amplitude are given by the maximum of this landscape. The population exchange is periodic and thus there are many maximums but the one corresponding to the shortest i-SWAP gate in our case of negative J, is the first one. The optimal gate parameters can be extracted from the data set by fitting a sine to each time-line. Then the maximum of the frequency vs. qubit detuning relation is found by fitting a parabola as shown in Figure 5c. The extremum of the parabola corresponds to the optimal gate configuration.

To confirm that parameters given by the method really give the i-SWAP we have simulated the corresponding landscape and compared it with the fidelity landscape. The Chevron landscape is simple to evaluate by applying $(\sigma_x \otimes \sigma_0)U_{bare}(\sigma_x \otimes \sigma_0)$ to the ground state $|gg\rangle$ and calculating the expected value of the measurement operator 1.15 $\langle M \rangle$ for the output state. The average gate fidelity is defined as

$$F_{i\text{-SWAP}} = \frac{\left|\mathrm{Tr}\left[U_{i\text{-SWAP}}^{\dagger} U_{bare}\right]\right|^2 + \mathrm{Tr}\left[U_{bare}^{\dagger} U_{bare}\right]}{20} \tag{2.1}$$

which does not require U_{sim} to be unitary [Pedersen 08]. The fidelity landscape and comparison of its maxima with simulated Chevron pattern for the parameters near i-SWAP gate is shown in Figure 2. From the good agreement of these landscapes we conclude, that the Chevron pattern is a good guide in finding the optimal gate parameters.

The fluxpulse parameters obtained from data shown in Figure 5c are precise enough, but such a measurement takes 1.5 hours. One could take less averages but the method is first order insensitive near the optimal configuration and the data extracted from far from resonance suffers from systematic errors due to other nearby avoided crossings.

Instead of measuring a large set of configurations we can use the gradient-free numeric optimization algorithm Nelder-Mead[9]. In our case we need to optimize the values of two parameters and the objective function corresponds to $\langle M \rangle$. The algorithm starts by measuring the values for 3 start configurations forming a triangle on a 2D plain. Then the configuration giving the worst value for the objective function is determined and three new configurations are measured:

- the center of gravity of the triangle,

[9]It has already been used in similar situations before in [Magesan 12] and [Kelly 14].

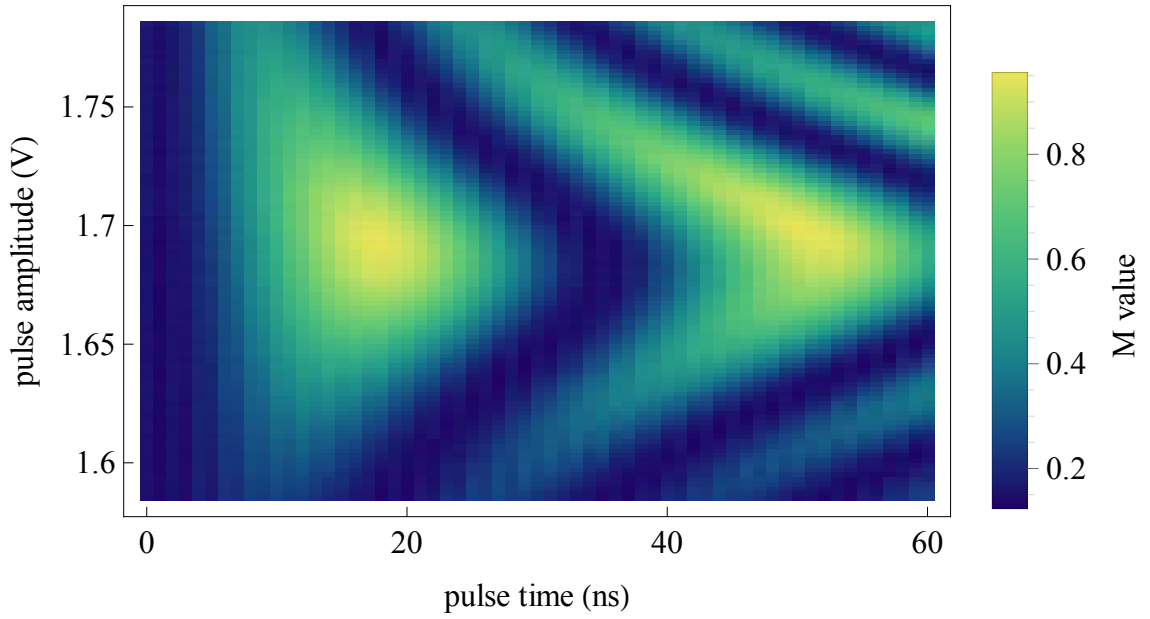

(a) M-value measured in the experiment, where length and amplitude of the square flux pulse was varied. The formed pattern is called the *Chevron pattern*.

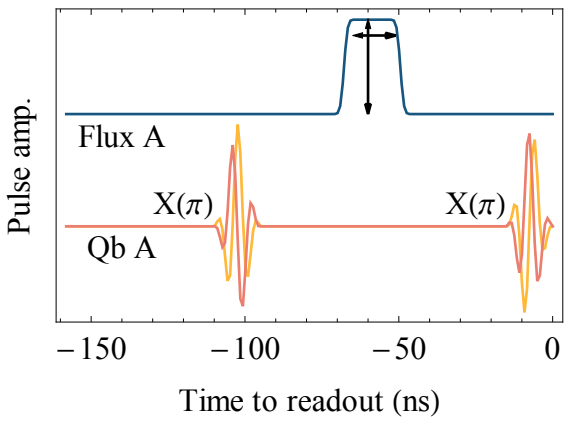

(b) Used MW and flux pulses.

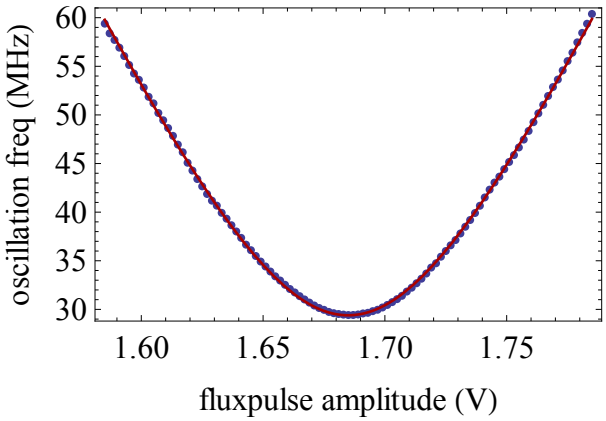

(c) Finding the optimal flux pulse amplitude.

Figure 5: Chevron pattern measurement experiment for calibrating the *i*-SWAPgate. In Sub-figure 5b flux pulses and both quadratures of the MW pulses at the intermediate frequency before the up-conversion are shown. In Sub-figure 5c parabola fit to frequencies of each Chevron pattern slice of constant flux pulse amplitude is shown.

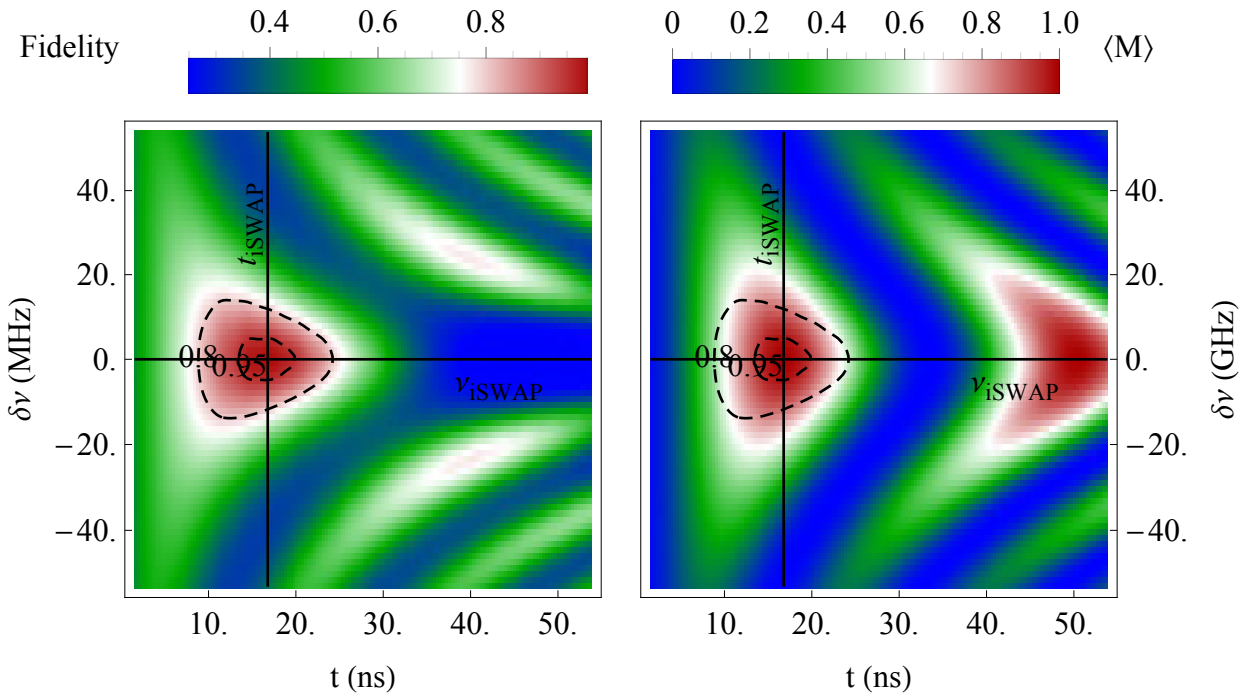

(a) Simulated *i*-SWAP fidelity landscape.

(b) Simulated chevron landscape.

Figure 6: Comparison of *i*-SWAP gate fidelity and Chevron pattern as function of detuning from resonance $\delta\nu$ and length of the interaction t. The optimal values are marked with solid grid lines. Contour corresponding to fidelity 0.8 and 0.95 are marked with dashed lines.

- the point which is the reflection of the worst value by the axes formed from other two and
- another point farther away in the same direction.

Then the new triangle is formed from the best two of the initial configuration and the best one out of the new configurations. Note that the triangle can expand, contract or shift depending on the gradient of the landscape. The cycle is repeated until the difference between three configurations gets below the desired value. In our case we reach easily the limit set by our AWG resolution with around 15-25 iterations. The used *Tektronix* AWG 5014 has time resolutions of 0.84 ns for 14-bit analogue output and the full range was used for best effective resolution. Due to filtering the amplitude resolution also improves the effective time resolution by approximately factor of two. The formed landscape and history of convergence are illustrated in Figure 7. This closed loop optimization routine was implemented using the multi-qubit operation support of the experiment control software *QubitCalib* [Heinsoo 13].

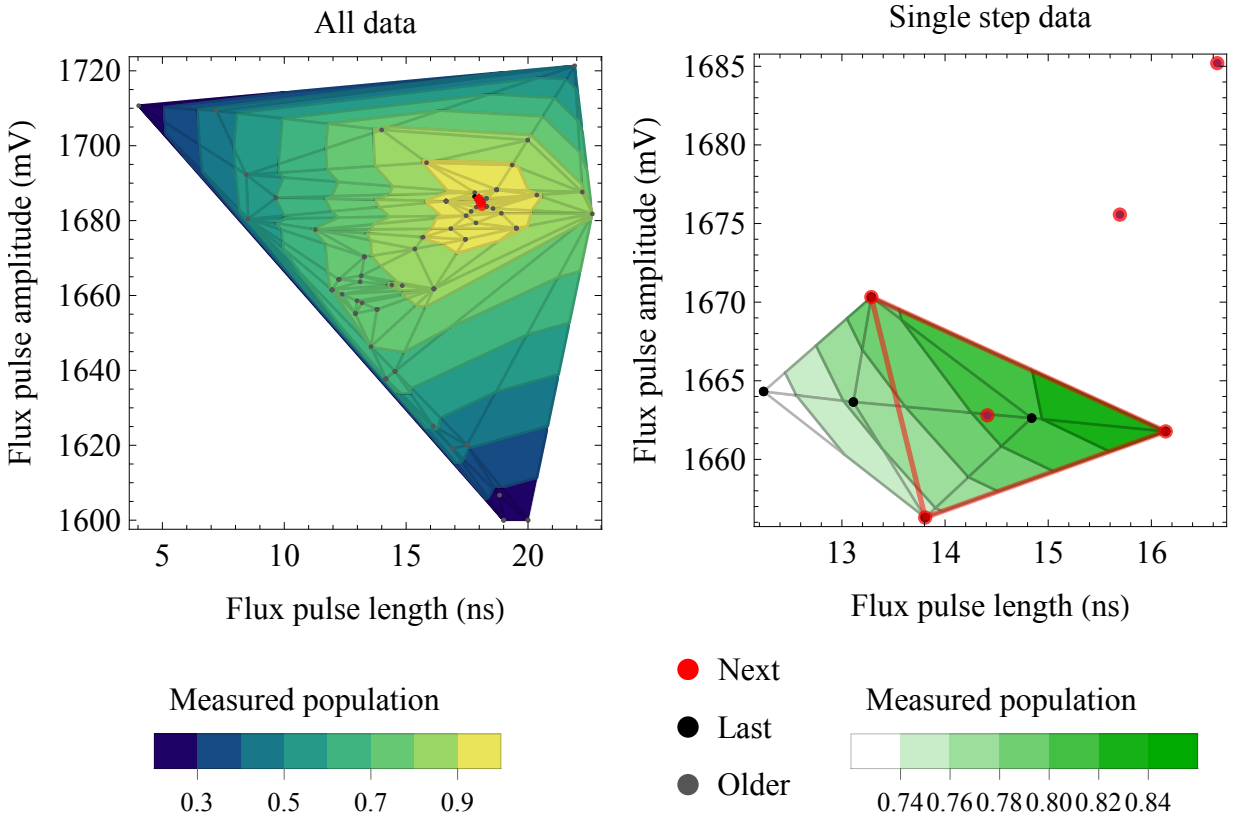

(a) Full landscape formed by measured data during NM optimization.

(b) Single Nelder-Mead algorithm step.

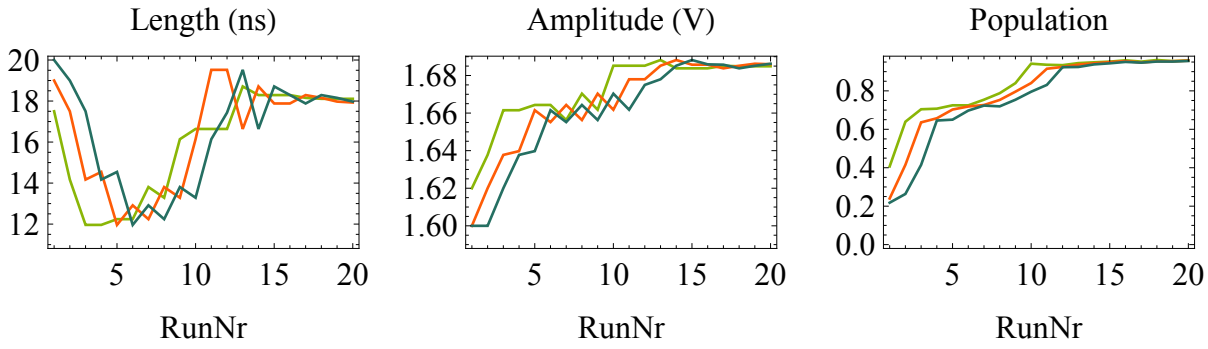

(c) Time lines of the optimized parameters (flux pulse length and amplitude) and of the objective function (measured two qubit population).

Figure 7: Nelder-Mead optimisation of flux pulse length and amplitude on the Chevron pattern landscape. The convergence of the method is seen from the fact that the next measurement configurations converge into a single point in the full data map 7a and into single lines in the time lines 7c.

2.2 Flux screening

If subsequent measurements with the device can be considered independent of each other then the result does not depend on the measurement repetition rate. It had been noticed before, that if in case of experiments with flux pulses the repetition rate was shorter than 100 µs compared to the usual 12.5 µs, the qubits seemed to have some additional detuning which depended on the repetition rate.

To characterize the flux induced detuning in the subsequent measurement we did sequence of Ramsey type of measurements after a flux pulse. A single Ramsey type of measurement consists of two $\frac{\pi}{2}$-pulses with a fixed delay in between. The first one takes the qubit from a ground state $|g\rangle$ into a superposition state $(|g\rangle + |e\rangle)/\sqrt{2}$. If the qubit is detuned from the rotating reference frame (RRF) the super position state evolves around the Z axes of the Bloch sphere similar to Larmor precession of spins in a magnetic field. In the end of the delay time the qubit has collected a phase ϕ and is described by a state vector $(|g\rangle + e^{-i\phi}|e\rangle)/\sqrt{2}$. The second $\frac{\pi}{2}$-pulse would take the qubit to an exited state $|e\rangle$ only if the qubit was not detuned[10]. In order to measure the phase shift, the phase ψ of the second $\frac{\pi}{2}$-pulse is varied and the qubit is read out to be in exited state $|e\rangle$ in case the phases of second Ramsey pulse and qubit precession are equal $\psi = \phi$. Ramsey type of measurements in the context of single-qubit IF calibration are discussed in [Baur 12, Menke 13].

By doing this measurement at several different waiting times after flux pulse, the time line of the detuning of the qubit can be studied. To see effects on a time scale a lot longer than our usual experiments the so called *over-trigger* scheme was used, where many AWG waveforms the with Ramsey scheme followed by a single waveform containing the flux pulse. Usually we assume, that the experiment trigger period is long enough to consider experiments to be independent.

The measured time line of the residual detuning from the flux pulse is shown in Figure 8. The result indicates an exponential decay with characteristic time scale of 21 µs and thus the effect of the flux-pulse can still be seen after 200 µs. It has been discussed before [Baur 12, Oppliger 12] that it could be due to a decaying screening current induced by the fast flux pulse.

We managed to suppress the effect with a simple compensation scheme shown in Figure 9a. Instead of one, we use two square flux pulses with equal length and amplitude, but with opposite sign. The second pulse induces the equal counter current and thus eliminates the seen exponentially decaying detuning. The time line measured after such screening compen-

[10] It could have also gathered a phase shift of multiple of 2π, but this corresponds to having the Ramsey delay too long and we assume this not being the case.

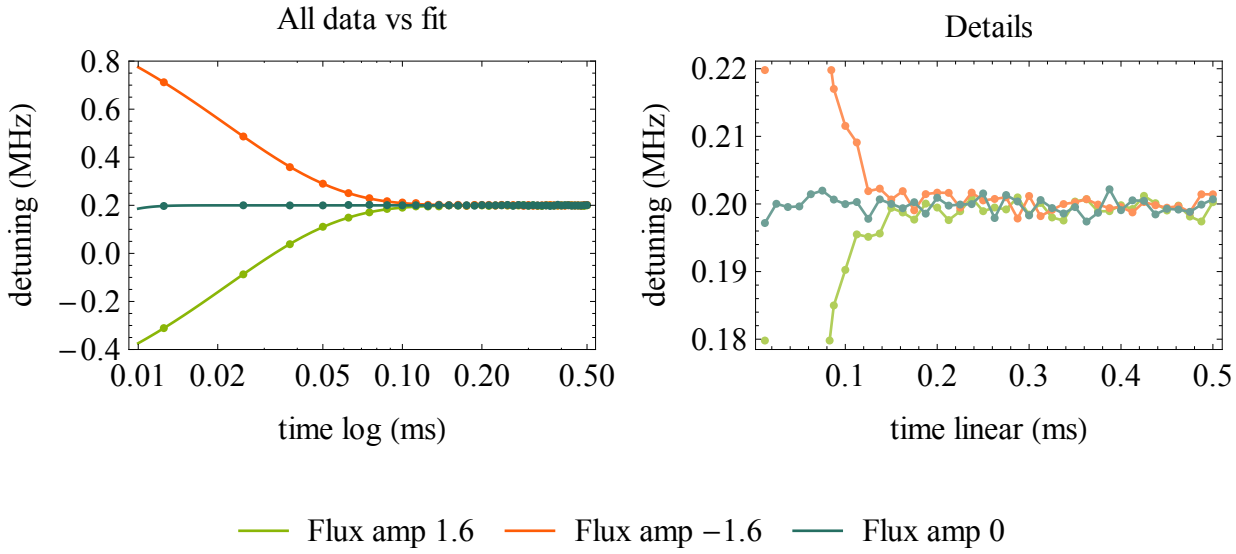

Figure 8: Time line of the qubit detuning after the flux pulse in case of three different pulse amplitudes: negative, positive and no flux pulse. The solid lines on the left plot are fitted exponents with decay times of 21 µs. The right plot shows the details of the data. The standard deviation of data points is in the order of fast data fluctuations as expected, but is not shown for clarity.

sated flux pulse is shown in Figure 2. Now it is feasible to have several flux pulses in a single experiment. In addition we can now decrease the length of the measurement iteration 8 times from 100 µs up to 12.5 µs and use the same time to take more averages leading to an increased measurement fidelity.

It is clear from the data shown in Figures 8, that the detuning does not decay to below measurable level, but goes to some constant offset. This effect is there even in the case the single qubit drive frequency had been calibrated just before the experiment. As we see the same offset in the experiment segment without the flux pulse the characteristic time scale of the effect has to be a lot longer than what we propose to be the decay of screening current. In addition to some environment induced instability of the qubit, for example variations in external magnetic field, it has been proposed in [Oppliger 12], that the flux pulses could heat the relevant area on the sample which in turn affects the qubit frequency via spin ordering in the superconductor [Sendelbach 08]. In either case it needs further study in the future. In order to avoid the screening current in the first place the ground planes could be moved further away from the qubit[11].

[11] It is not discussed, but seems to be done for example in [Vesterinen 14, Saira 13].

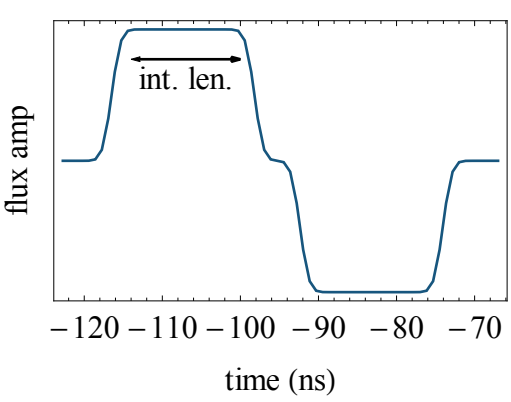

(a) Flux pulse shape which compensates the screening current using a mirrored shape.

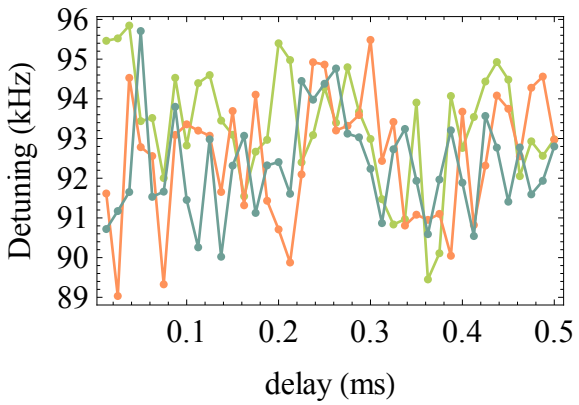

(b) *Over-trigger* ringing measurement with screening current compensation.

Figure 9: Data in Figure 9b shows, that the flux pulse shape shown in Figure 9a does compensate the 21 µs decay seen in Figure 8. The difference in the constant offset was probably due to recalibration of the IF between these two experiments. Apart from that the experiments were identical. The *Interaction length* of the flux pulse is marked in Plot 9a. The origin of the time axes is the same in bot plots, but note the difference in units.

2.3 Flux pulse ringing

It is important to have no remaining detuning after each individual flux pulse to be able to consider successive flux pulse based gates independent. When the long time scale effect shown in the previous section has been compensated we can focus on the qubit frequency response closer to the flux pulse. For this we use a method similar to over-trigger Ramsey described in previous section, but now the Ramsey measurement is done in the same waveform as the flux pulse - it is *iso-trigger*. Again the distance between the Ramsey scheme and flux pulse is varied. The qubit detuning time lines for three different flux pulse amplitudes are shown in Figure 10. Such a method for studding the flux pulse detuning after a flux pulse was also described in [Barends 14, Supp.] and similar observations, although obtained a different way, have been discussed in [Johnson 11].

As can also be seen from Figure 10 it takes around 50 ns for the detuning to reach a level less than 1 MHz. Then the detuning is order of magnitude smaller from the spectral width of the applied MW pulses. Detunings less than 1 MHz will not decrease the fidelity of single-qubit operations too much and only contributes to the single qubit phase errors. As will be described in Section 2.4, single-qubit PHASE gates are anyway need on both sides of the

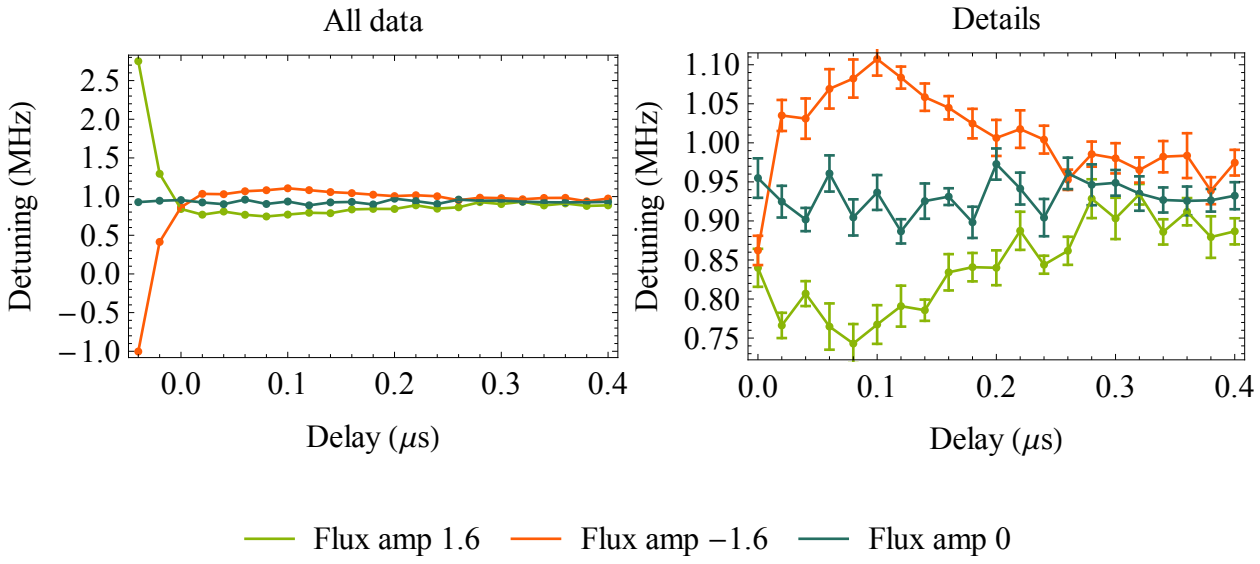

Figure 10: Three time lines of qubit detuning recorded in an *iso-trigger* flux pulse ringing measurement show fast decay, small undershoot and a constant offset. Note that the flux pulse scheme includes a *spacer-after* of 75 ns and the time axes is relative to this point.

flux pulse. The way they will be calibrated will also compensate for the small phase errors collected during the detuning from the steady state. It is important, that detuning is not accumulated over several operation blocks as would the uncompensated screening current. Thus an additional waiting time to the 75 ns spacer already shown in the pulse scheme in Figure 10, is not needed.

The origin of the undershoot and the slow decay of the detuning has several possible sources. When generated, the flux pulses are inverse filtered to compensate the response of AWG and cabling [Bozyigit 10]. It is not possible to measure the response for inverted filter in the actual measurement setup. Dipstick measurements indicate that the response does depend on the temperature of the cables [Baur 12, Ch. 4] and this might introduce the imperfection. It has been proposed, that the ringing comes from a standing wave in some later stage of the cabling [Barends 14, Supp.] (for example between sample holder connector mount and sample connections) and can be compensated by adding a exponential term into the measured warm cabling response. In [Ghosh 13] it is discussed, that adiabatic flux pulses loose significantly less population into other nearby non-computational states and it would also decrease the requirement on the precision of the inverted filter. On the other hand during adiabatic tuning of qubit frequency, the qubit might cross other decay channels. The finding of the sweet spot

between these two effects and other possible solutions are yet to be tried.
In addition to the side effects just described, the detuning does not decay to below the measurement precision, but to a constant offset. Possible reasons for this are described in end of Section 2.2.

2.4 Dynamic phases

In an experiment the rotating reference frame (RRF) has to be well defined, to have a chance of controlling the phases of the qubit states. The frequency of the reference frame corresponds to the qubit transition frequency to the first exited state. In our case, we fix the LO and fine tune the IF using a Ramsey type of measurement [Menke 13, Baur 12]. The RRF phase is the sum of LO and IF phases. Phase of IF is fixed by reused control-software generated AWG waveforms. Single-qubit experiments are easy in the sense, that LO phase can be arbitrary in each experiment segment. This is because all MW control-pulses of the single qubit have phases defined by the same LO which defines the temporary computational bases and the used dispersive readout is phase insensitive (measures only σ_z component).
In case of two-qubit gates the flux pulses are done at some fixed point after the start of the experiment and it takes the qubit state from two different RRFs into a single one. Now the relative phase of qubits can not be random over experiments. To have fixed LO phase in the beginning of the experiment segment it is chosen to be commensurate with the experiment repetition rate[12]. To keep the relative phase of the qubits fixed the LO-s and the experiment trigger are phase-locked. To choose the relative phase of the qubits in the beginning of the qubit-qubit interaction (the end of the finite rise time of the flux pulse) we do a single qubit PHASE gate. This is done by tuning a height of the buffer on the rising edge of the flux pulse. Similarly the qubit has to be taken back to its original RRF in the end of the interaction with a buffer on the falling edge. The buffers also suppress side effects of rapid flux pulse amplitude changes induced by AWG non-linearity. The phases the qubit collects in the other RRF are called *dynamic phases*.
In the experiment there are several cases were the LO phases shift[13]. In this case a simple dynamic phase calibration procedure is done which in case of the i-SWAP operation is easy to interpret. First one of the qubits is prepared in the superposition state with a $\frac{\pi}{2}$-pulse. Then a well calibrated i-SWAP gate would swap the state into the second qubit adding a phase shift of 90°. The $\frac{\pi}{2}$-pulse with phase shift of 90° on the now populated qubit should set it into

[12] We mostly use a trigger rate of 25 µs.
[13] For example the trigger generator phase shifts in relation to reference signal after a change of settings or a restart.

the exited state. If the corresponding buffer amplitude is varied the maximum population marks the optimal configuration. Due to the similarity to the experiment described in the previous section, the scheme is referred to as *cross-qubit Ramsey* type of experiment. The pulse scheme is shown in Figure 11.

Note that we also have to vary the corresponding buffer in the screening current compensation pulse to keep the total area under the pulse constant. As the qubit frequency dependence on the magnetic field shown in Figure 3 is linear for the small detuning from the parking position, the buffer after the flux pulse effectively compensates itself. For larger flux pulse amplitude the second order dependence has enough effect however and the method still works. This is demonstrated by the good fit of $\cos(x^2 + x_0)$ onto the experimental data shown in Figure 12. Note also, that as seen from Figure 11, the second buffer calibration is sensitive to the setting of the first one due to the screening current compensations scheme and for this reason the order of the buffer calibration is important.

2.5 Conditional phase

The first part of buffer calibration, where the buffer-before is calibrated to compensate the dynamic phase of the non-fluxed qubit B, should give a same result independently weather qubit B is initially exited or not. When we did such a experiment we did see a phase shift which corresponds to a *conditional qubit detunig* in order of 1 MHz[14]. From quantum process tomography experiments described later, we know that the effect is due to the residual qubit-qubit coupling. Even when tuned far from the resonance the coupling dispersivly shifts the qubits and the magnitude of the shift depends on the qubit states due to the qubit anharmonicity.

A similar problem is solved in nuclear magnetic resonance (NMR) quantum computation using *dynamic decoupling* [Nielsen 00, Ch. 7.7.3]. Although it is possible to implement it with only linear overhead in the number of qubits [Leung 00] it is still unfeasible with our T_1 and T_2 times. Instead we make use of the additional buffer in our flux pulse to implementing a conditional arbitrary phase (CARB-PHASE) gate.

The c-PHASE gate briefly discussed in Section 1.4 works by collecting a geometric phase during the closed evolution cycle through a non computational $|fg\rangle$ state. In the case of on-resonance oscillation the collected geometric phase is exactly 180°. In the off-resonance amplitude and period of the population are smaller and the collected geometric phase differs from the on-resonant case. By choosing a correct length and amplitude of the additional flux

[14]This has nothing to do with the anomaly described in Section 2.3 as then neither of the qubits was initially exited.

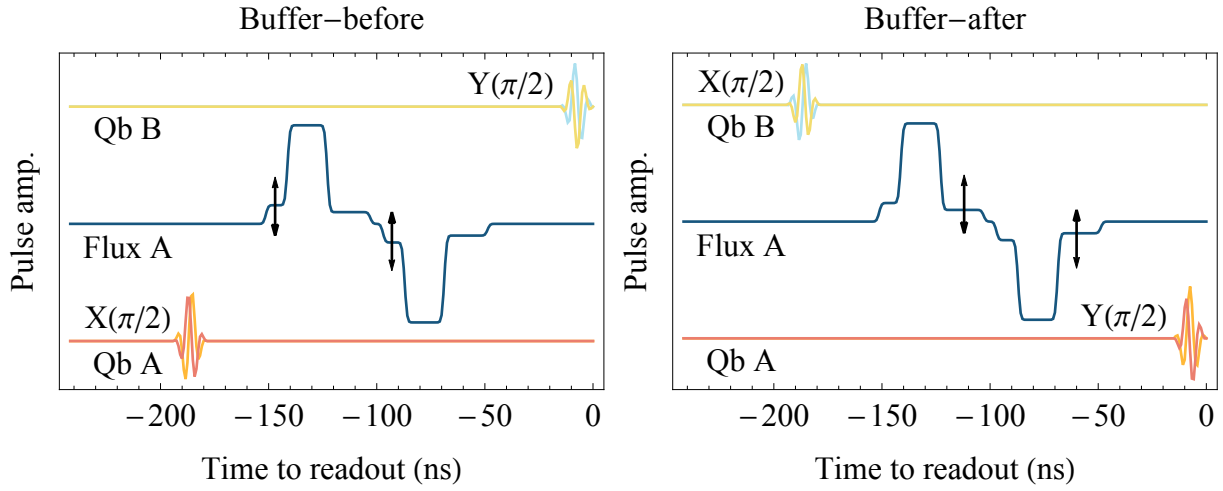

Figure 11: Pulse scheme for calibrating the dynamic phase compensations using two buffers. LO modulated MW drive waveform for qubits A and B are shown together with the flux pulse shape for detuning qubit A. On the left (right) plot the buffer before (after) is varied and the resulting phase error is turned into measurable qubit population by the $\frac{\pi}{2}$-pulses. As we use the inverted flux pulse shape to compensate for the induced screening current the corresponding buffer in the inverted pulse also varies.

pulse buffer we could compensate an arbitrary conditional phase while also recovering all of the population into two qubit subspace. The new flux pulse shape with multiple buffers is shown in Figure 13.

To compose a similar fidelity landscape to the one shown in Figure 6 we assume, that the optimal flux pulse interaction amplitude and length are chosen as described in Section 2.1 corresponding to

$$U_{i\text{-SWAP}sim} = U_{bare}(t \to t_{i\text{-SWAP}}, \theta \to \theta_{i\text{-SWAP}}). \tag{2.2}$$

where the U_{bare} is the propagtion operator of simulated Hammiltonian in RRF of bare qubits defined in Equation 1.14. In this RRF the single qubit states collect phases corresponding to definition of the i-SWAP gate. In addition the choice of RRF makes $|ee\rangle$ state collect the conditional phase we are going going to compensate with the new buffer.

The evolution after the i-SWAP operation we look in the RRF of the dressed states to avoid any other phases, but the geometric. The CARB-PHASE buffer with a amplitude θ and length t is given simply by $U_{dressed}(t, \theta)$ defined in Equation 1.14. To make the simulations with different buffer lengths comparable the we add the evolution of the system in its parking

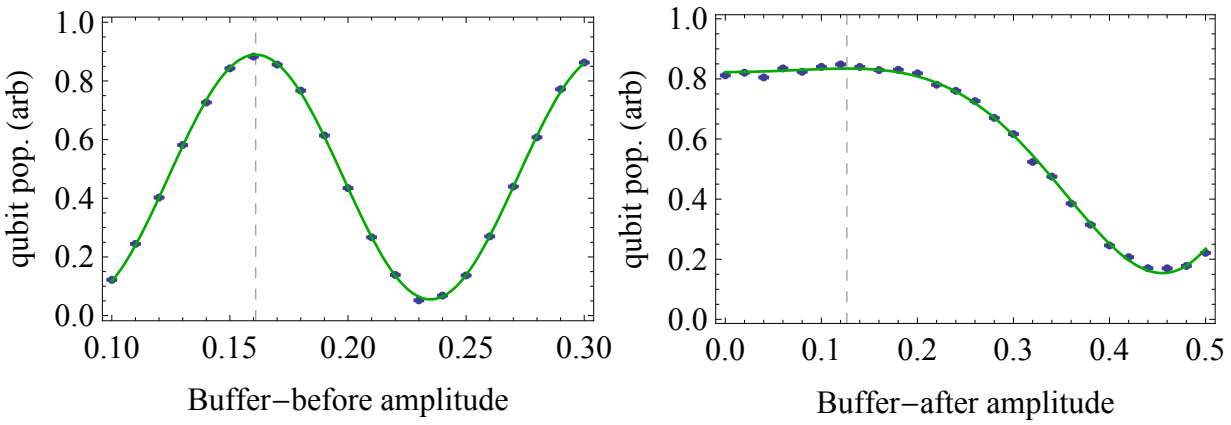

Figure 12: Measured qubit population in the dynamic phase calibration experiment. The maximum qubit population is seen in the case of flux pulse buffer configuration corresponding to the i-SWAP gate. The buffer amplitude marked with gray dashed line will be used. It is also clear, that the response is linear in buffer amplitude in the case of the first buffer and second order sensitive in the case of the second buffer as the functions $\cos(x + x_0)$ and $\cos(x^2 + x_0)$ fit the data well for the buffer before (left plot) and after (right plot) respectively.

position till the end of the simulation and define it by

$$U_{\mathbb{1}sim} = U_{dressed}(t' \to t_{max} - t, \theta \to \theta_{parking}). \tag{2.3}$$

To see the relevat dynamics it is enough, if the length of the simulation $t_max = 225\,\text{ns}$. Now we can write down the total process of conditional phase compensation ($CComp$) as

$$U_{CComp} = U_{\text{CARB-PHASE}}(\phi_{zz})\, U_{\mathbb{1}sim}(t)\, U_{dressed}(t, \theta)\, U_{i\text{-SWAP}sim} \tag{2.4}$$

where ϕ_{zz} is the conditional phase additional to the one collected by $U_{\mathbb{1}sim}$ and $U_{i\text{-SWAP}sim}$. Using this result, the fidelity to ideal i-SWAP operation can be evaluated again by usage of Equation 2.1.

From Figure 14 it is clear, that in our system the fidelity improvement by the added buffer is significant. Note how the shortest high fidelity conditional phase compensation buffer for the $\phi_{zz} = 110°$ has to be quite close to the complete c-PHASE gate. In case of $-50°$ one gets a total gate fidelity above 80% also in case of doing nothing, but a buffer is needed to achieve higher fidelity. In the experiment the optimal configuration for the conditional phase compensation buffer can be found with a similar method to the one described in Section 2.1 and is currently under development.

There are other ways to suppress it, but they all have some important pay-offs. By choosing parking frequencies farther from the resonator or decreasing the qubit coupling to resonator

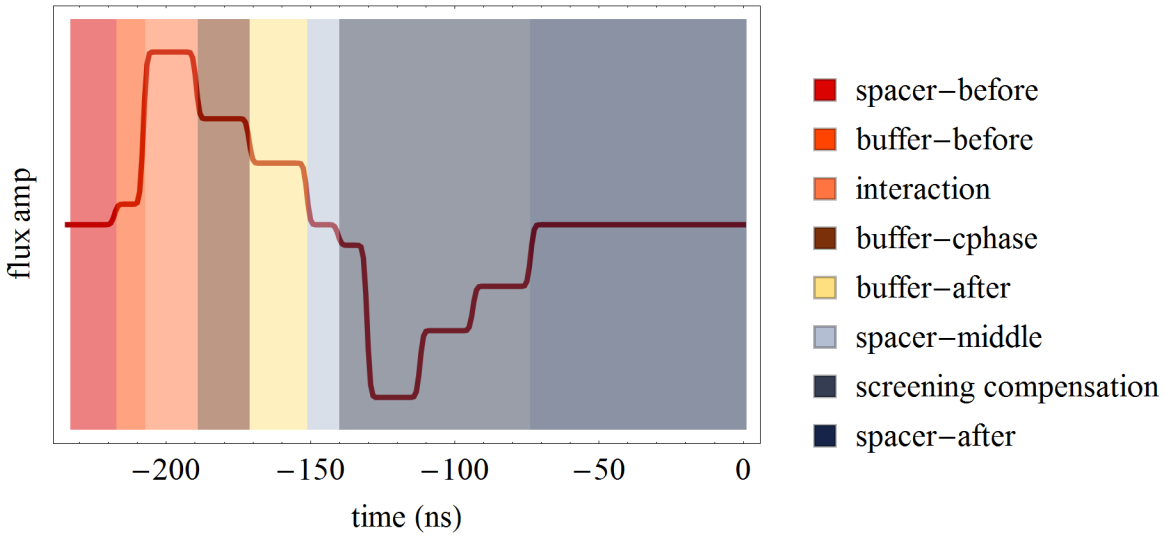

Figure 13: Final flux pulse shape with different regions shaded according to the corresponding usage.

by sample design we would decrease the J at the resonance more, than it would decrease the residual coupling in addition to decreasing the speed of dispersive readout. If we just used bigger qubit parking frequency difference it would improve the on-off ration of the coupling, but we would loose in the relative accuracy of the AWG both in amplitude and time (relative RRF frequency would increase) where we already are at the limit.

Compensating the conditional phase is vital to realise the algorithmic approach described in the introduction of the present chapter. So far this problem has been hidden by decomposing the two-qubit operations into c-PHASE or equivalently c-NOT gates. When the c-PHASE gate is fine tuned to give correct conditional phase, one actually calibrates the flux pulse into CARB-PHASE operation which together with residual conditional detuning gives the desired c-PHASE operation. When screening current compensation is not used, the plain c-PHASE gate has a typical length of 20 ns and even with some buffers the waiting time is too short to really notice the difference of CARB-PHASE and exact c-PHASE gate. Also when the i-SWAP was not used, the parking position off qubit A could be farther from the avoided crossings and thus the on-off ration of c-PHASE gate could be improved without loosing relative AWG resolution.

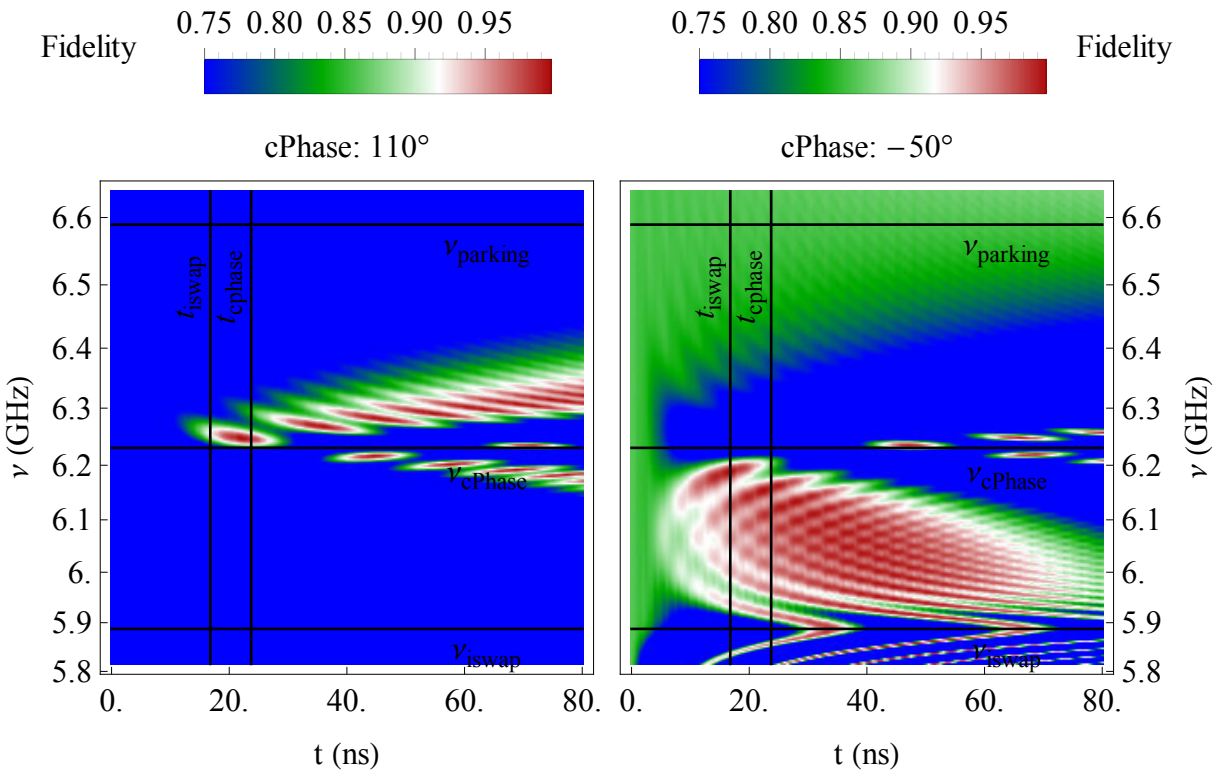

Figure 14: *i*-SWAP fidelity landscapes for the cphase-buffer parameters for two different conditional phase values. For comparison the *i*-SWAP and c-PHASE gate lengths and corresponding qubit detunings together with qubit *A* parking positions are marked with solid lines. Note, that the detuning axes are non-linear, as the actual control parameter is the flux pulse amplitude which is plotted linearly.

2.6 Discussion and outlook

As mentioned in the introduction of this chapter also the two-qubit identity process $\mathbb{1}$ suffers from this problem. For example this is why in the *Quantum von Neumann Architecture* discussed in [Ghosh 13] simultaneous excitation of coupled qubits is forbidden while doing single qubit operations. Unlike in the case they discuss, in our current designs we have no memory resonators and the approach is not applicable. Instead of staying in the single excitation manifold one could calibrate the $\mathbb{1}$ operation like any other by finding the optimal flux pulse for a compensation CARB-PHASE gate.

As seen from Figure 13 the resulting pulse scheme is already rather complicated. In a realistic setup the assumption that different features of the pulse shape can be calibrated independently might not hold. One could insert all of the calibration parameters (or use a more general flux pulse model) into a single closed-loop optimization scheme like ORBIT [Kelly 14],

where again the Nelder-Mead model free optimization method is used. However they are able to implement randomised benchmarking (RB) due to having order of magnitude better T_1 and T_2 than we do at the moment and use the RB fidelity as an objective function. Instead of this, one could develop more direct error syndrome measurements or use Monte-Carlo process certification [Steffen 12].

If the relevant experimental side-effects could be estimated quantitatively with good precision, one could employ algorithms like GRAPE [Khaneja 05] to optimise the pulse shape for a given Hamiltonian for maximal gate fidelity, shortest possible length and possibly maximal error-resilience [Egger 14a, Egger 14b]. However the only side-effect we can predict from a relatively simple Hamiltonian is the conditional phase we just discussed and the method would probably not improve the i-SWAP gate. On the other hand it is possible to implement more complicated gates with complex qubit control and the optimal pulse control would help to adjust the pulse shape for the dynamics of the system.

3 Process tomography

Tools of quantum process tomography are intended for partial or full characterisation of a *quantum black box*, of an unknown quantum gate. It can be used as a method to diagnose the errors or to quantify the goodness of the implemented gate. In turn it relies on the ability to carry out quantum state tomography, a full characterisation of quantum state, in addition to the ability of precisely preparing input states.

For detailed discussion on state tomography refer to [James 01], which also includes discussion on maximum likelihood, or to [Liu 05] for an extensive theoretical overview of state tomography of superconducting qubits. The full process tomography was first described in [Chuang 97] and later revisited in [Leung 03]. Recent publications cover partial process tomography [Wu 13] and optimization in case of additional assumptions [Baldwin 14].

Here I will discuss several different representations of a quantum process, which were useful for the study of relevant errors. All of the methods below were programmed in the *Wolfram Language* in a reusable manner for the future study of a larger set of quantum operations. Here I only present data for the i-SWAP and two-qubit identity ($\mathbb{1}$) gate. Note, that the $\mathbb{1}$ process is not trivial, due to the small coupling of $|ee\rangle$ and $|fg\rangle$ levels at our parking position introducing a conditional phase shift discussed in Section 2.5.

The examples of experimental data will be limited to three data sets featuring nearly best $\mathbb{1}$ and i-SWAP gates we can do and, for demonstration, a $\mathbb{1}$ gate which does not include conditional phase compensation. The data sets will be referred to as `good-`$\mathbb{1}$, `good-`i-SWAP and `bad-`$\mathbb{1}$ accordingly. Detailed numerical comparison of the data sets is provided in Appendix B and experiment configurations are given in Table 1.

3.1 Two-qubit readout and state tomography

In order to show the reconstruction of an unknown two-qubit state, few details about our readout scheme need to be discussed. The general principle of the dispersive readout was outlined in Section 1.6. Here I will describe the relevant details about the way the full information of the qubit state is gathered from the measured homodyne signals.

Each experiment sequence includes segments consisting of the measurement calibration time traces. For these, the qubits are prepared in the σ_z eigenstates $Z_\pm \otimes Z_\pm = \{|gg\rangle, |ge\rangle, |eg\rangle, |ee\rangle\}$. The homodyne measurement records the time dependence of both quadratures of the transmitted signal. If the phase of the measurement tone was chosen such, that in the case of the $|gg\rangle$ state the Q-quadrature is carrying most of the signal, the normalised transmitted signal

strength in the quadrature is [Filipp 09]

$$\alpha_{\pm\pm} = -\kappa \left\{ (\kappa/2)^2 + (\Delta_{rm} \pm \chi_1 \pm \chi_2) \right\} \tag{3.1}$$

with $\pm$ corresponding to the prepared eigenstates $Z_\pm$, $\Delta_{rm} = \omega_r - \omega_m$ is the readout frequency ω_m detuning from the resonators bare frequency ω_r and χ_i denotes the dispersive shift of the qubit i. In the experiments throughout the thesis the readout frequency was chosen to be $\omega_m = \chi_1 + \chi_2$ such that the maximum transmition corresponds to the ground state $|gg\rangle$. From the calibration traces we extract scaled and normalised $\alpha'_{\pm\pm}$ by

$$\alpha'_{\pm\pm} = 1/N \int_{t_m}^{T} \left[\langle M(t) \rangle_{\pm\pm} - \langle M(t) \rangle_{++} \right] dt \tag{3.2}$$

where $\langle M(t) \rangle$ is the ensemble average of the signal for a given time t in the experiment and N we chose such that the exited state response $\alpha'_{--} = 1$. This gives an effective measurement operator

$$M = \begin{pmatrix} 0 & 0 & 0 & 0 \\ 0 & \alpha'_{-+} & 0 & 0 \\ 0 & 0 & \alpha'_{+-} & 0 \\ 0 & 0 & 0 & 1 \end{pmatrix} = \begin{pmatrix} 0 & 0 & 0 & 0 \\ 0 & m_{eg} & 0 & 0 \\ 0 & 0 & m_{ge} & 0 \\ 0 & 0 & 0 & 1 \end{pmatrix} \tag{3.3}$$

where at the last equality the notation is changed back to the one used in Section 1.6. Note, that we can assume the M to be diagonal as we can consider the dispersive readout to be a non-demolition measurement [Blais 04].

A general n-qubit state (might be a mixed state) with global phase degree of freedom, is described by $4^n - 1$ real parameters. Thus to fully characterize a quantum state the number of real parameters corresponds to the number of linearly independent measurement basis needed. Although we have the measurement calibration traces, which should normalise the measurement signal, they have the preparation pulses just before the readout and are measured in an experiment segment without any other pulses. The state tomography might be done in a segment with flux pulses or at some earlier time before the measurement compared to the measurement calibration. To take this into account we always did in total $n_{sTom} = 16$ measurements. This over-completeness enforces the correct normalization providing the information about the states pureness. It is easy to see in the single-qubit case, where three linearly independent measurements only give the direction of the Pauli state-vector in the Bloch sphere[15]. Without the additional fourth measurement (or relying on the calibration of the sensitivity of the measurement apparatus) it is not possible to tell if the vector is pointing

[15] See Appendix A.

onto pure states represented by the surface of the Bloch sphere or whether the measured state corresponds to a mixed state inside the sphere.
As the measurement operator measures only the σ_z component, one needs to prepend the readout with a unitary transformation U_k to rotate the other components of the state vector to the measurement axes. If the rotation axes (eigenvalues) of U_k span the full studied subspace, this gives the information

$$\langle M \rangle_k = \mathrm{Tr}\left[U_k^\dagger M U_k \rho_q\right] \tag{3.4}$$

about all of the degrees of freedom for the reconstruction of an unknown state ρ_q. The goal of state tomography is to turn the 16 measured values $\langle M \rangle_k$ into some common representation of the state. The task is described with a linear equation

$$\langle M \rangle_k = A_{kl} r_l \tag{3.5}$$

where indexes $k, l \in [1 \ldots 16]$. If r_l are the coefficients of the Pauli state-vector defined with a base

$$P_{ij} = \{\sigma_0, \sigma_x, \sigma_y, \sigma_z\}_i \otimes \{\sigma_0, \sigma_x, \sigma_y, \sigma_z\}_j \tag{3.6}$$

with $i, j \in [1 \ldots 4]$, the linear map A_{kl} will be defined as

$$A_{kl} = \mathrm{Tr}\left[U_k^\dagger M U_k P_l\right]. \tag{3.7}$$

Equation 3.5 is now solved for r_l by inverting the A_{kl} and the input state ρ_q is reconstructed by the superposition of the basis states

$$\rho_q = \sum_l r_l P_l. \tag{3.8}$$

Note, that it is easy to use any other representation by choosing a different basis for r_l. One can also do more measurements than there are coefficients r. In this case $\dim \langle M \rangle_k \neq \dim P_l$, thus A_{kl} is not a square matrix and therefore the pseudo-inverse A_{kl}^+ is to be used instead of the matrix inverse A_{kl}^{-1}. By doing the extra linearly dependent measurements one effectively averages over possible errors induced from imperfect measurement rotations U_k by least squares fit thus helping against systematic errors.

3.2 Optimizing the readout parameters

In the readout scheme within the quantum state tomography are two tunable parameters: measurement tone frequency ω_m and its phase. These parameters we fixed up to this point.

The later can be kept arbitrary, as we record the signal in both quadratures in the homodyne measurement. Instead of changing the phase of the readout tone, the recorded time traces can be rotated by an angle θ on the IQ plane before the projection onto the Q-quadrature axes.

Due to the scaling and normalisation of the effective measurement operator, both the readout frequency and the phase will only change the values of $m_{eg}, m_{ge} \in [0, 1]$. Tuning of the readout has an effect on the matrix A_{kl} defining the quantum state tomography. In order to find an optimal value for the described free parameters, one first needs a measure to quantify the usefulness of the choice. Here we discuss condition number $\kappa(A_{kl})$.

The condition number of a matrix A is defined as $\kappa = \|A\| \cdot \|A^{-1}\|$ where different matrix norms $\|\blacksquare\|$ can be used. The interpretation is especially simple in the case of the *2-norm* which corresponds to the maximal singular value. Then [Cheney 12]

$$\kappa_{2\text{-}norm} = \frac{\max[\text{sing}\, A]}{\min[\text{sing}\, A]}, \tag{3.9}$$

where sing A gives the list of singular vales of the matrix A describing the linear map. As singular values describe the scaling of eigenvalues by the transformation, the $\kappa_{2\text{-}norm} \in [1, \infty]$ describes the ratio of largest and smallest scaling coefficients. If $\kappa_{2\text{-}norm} = 1$, all of the eigenvalues are evenly scaled. If $\kappa_{2\text{-}norm} >> 1$, some eigenvalues are scaled considerably more and in case $\kappa_{2\text{-}norm} = \infty$, the transformation map A is singular, meaning the measurement results do not uniquely define the quantum state ρ_q.

It is obvious, that a readout phase and frequency giving very large $\kappa(A)$ would be a bad choice. Corresponding to the scaling interpretation of singular values, $\kappa(A) = 1$ corresponds to equal scaling of eigenvalues from the space of measurement results to the space of qubit state parameters and even distribution of errors, which is wished.

Shown in Figure 15a is $1/\kappa_{2\text{-}norm}$ as a function of m_{eg} and m_{ge}. It is clear, that $1/\kappa$ goes to 0 (meaning singular map A_{kl}) only when $|m_{eg}| + |m_{ge}| = 1$. Unintuitively $m_{eg} = m_{ge}$ or even $m_{eg} = m_{ge} = 1$ does not prohibit inversion of A_{kl}. Thus it is enough to distinguish a single two-qubit state from the rest in order to reconstruct the quantum states from the set of quantum state tomography measurements. The dots in Figure 15a represent a typical set of experimentally accessible configurations, where the readout frequency corresponds to the resonator frequency for the two-qubit state $|gg\rangle$ and only the quadrature projection angle θ is varied. The condition number as as function of the phase angle is also shown as 1D-slice in Figure 15b.

As all of the points, independent of θ, correspond to equally reasonable condition number, it is better to avoid a θ value, for which κ is very sensitive. These correspond to angles where

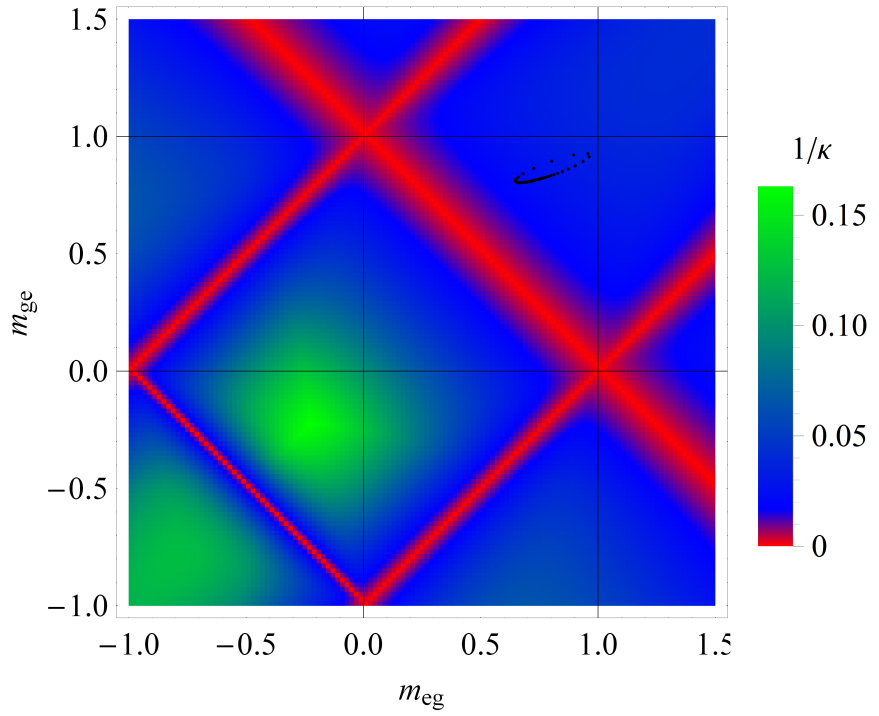

(a) Inverse of the condition number $\kappa_{2\text{-}norm}$ as a function of the scaled measurement operator M diagonal elements m_{eg} and m_{ge}. The red areas represent singularity of the linear set of equations for state tomography. The set of black points mark the configurations of a single experiment data, but a different phase θ.

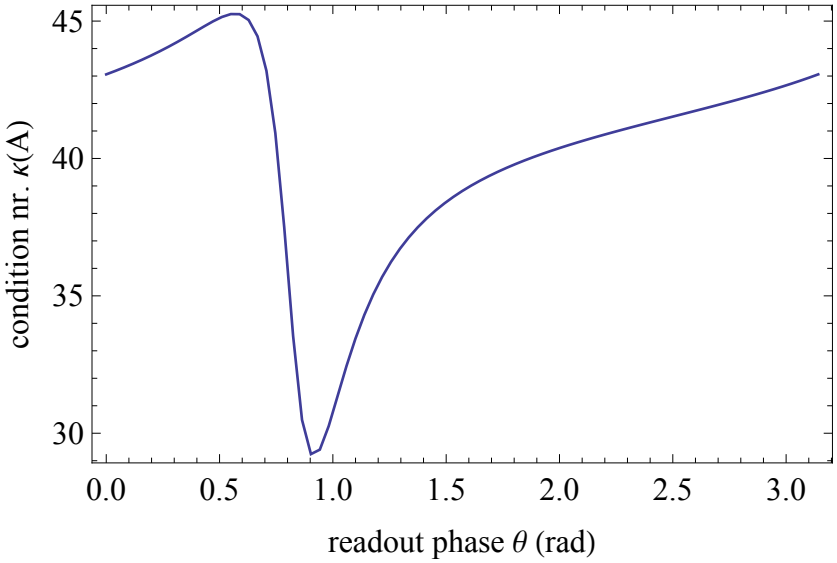

(b) Condition number of state tomography map A as a function of readout phase angle θ.

Figure 15: Study of optimal condition number.

the relative difference of the projected quadrature values are small and thus small variations in the measured quadrature values cause significant readout errors.
By projecting the two quadrature signal a into scalar value some information is lost. It is possible, to make use of all measured information, making the analysis more robust and sensitive. By making use of the acquired phase information it is possible to separate $|gg\rangle, |eg\rangle, |ge\rangle$ and $|ee\rangle$ in a single measurement. This has been done for example in [Steffen 13a]. This requires a more careful choice of readout tone frequency, a more complicated approach in data analysis and reformulation of state tomography. For the goals of the current thesis, the described analysis scheme gives clear answers and the readout improvement and error analysis is left as a task for the future.

3.3 Input-output map & error syndromes

In order to reconstruct the unknown quantum process, output states have to be measured for several input states. Here I present straight forward representations of the quantum process useful for debugging and as will be shown later, for finding efficient error syndromes.
The measurement value for rotated measurement operators M_k and prepared states ρ_l can be estimated by

$$\langle M \rangle_{kl} = \mathrm{Tr}\left[M_k U_{ideal} \rho_l U_{ideal}^{\dagger}\right] \tag{3.10}$$

and here we refer to such representation of the process as *input-output-map* (*io-map*). The examples for $U_{ideal} = U_{\mathbb{1}}$ and $U_{ideal} = U_{i\text{-SWAP}}$ are shown in Figure 16. For the examples given here, the diagonal components of the M operator are fixed to realistic values of $m_{eg} = 0.6$ and $m_{ge} = 0.8$, but in the case of each experiment they are recalibrated. Different measurement axes are achieved by single-qubit pulses, which rotate the measured state component to the measurement axes Z_+. Here $+$ denotes the σ_z eigenstate corresponding to positive eigenvalue (ground state) corresponds to $\langle M \rangle > 0$ and negative to $\langle M \rangle = 0$ and the other way around for Z_-. Thus measurement of Z_+ gives a maximum separation for the ground state for the values of m_{eg} and m_{ge}. The examples given in Figure 16 contain measurements with both $+$ and $-$ readout rotations. Although they contain the same information in a perfect system, one of them gives better contrast due to the M not being invariant under qubit state flip σ_z. Having better contrast less averaging copies are needed and this saves measurement time. On the preparation side $+$ $(-)$ denotes that eigenstate corresponding to the preparation of a state with a positive (negative) eigenvalue of the corresponding Pauli operator.
The io-map representation is helpful when debugging the early stage of the experiment. When one compares the data to simulations, it is easy to recognize specific problems in any preparation or measurement rotations as they lead to a difference of a whole column

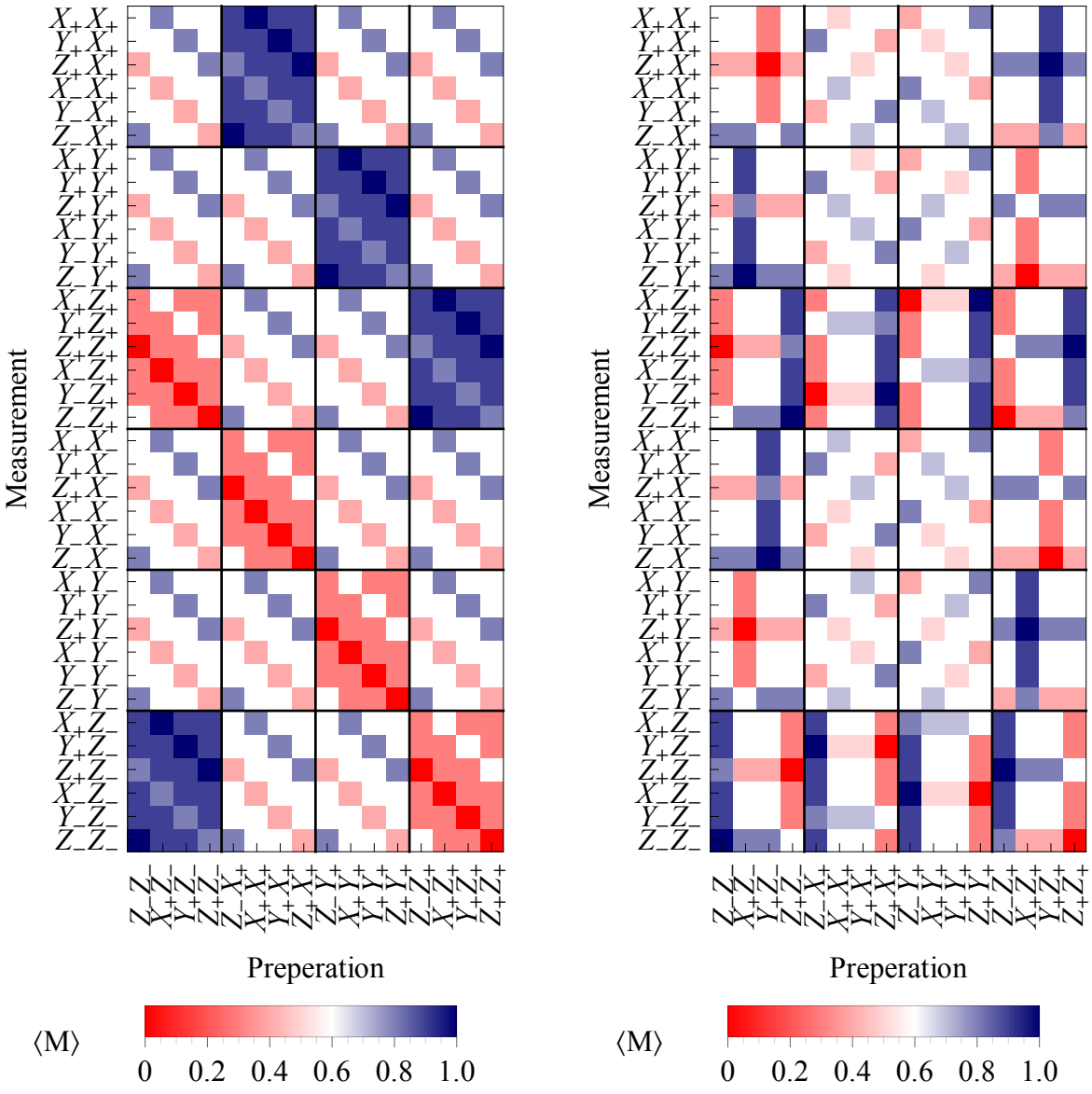

(a) io-map of the $\mathbb{1}$ process

(b) io-map of the i-SWAP process

Figure 16: Example of theoretical input-output maps. Labels on horisontal axes mark different preperation states and on vertical axes are the measured components (see main text). Colours represent the expected measurement operator M values.

or row comparing to the simulation. The pour contrast of Z component readout elements of the matrix could be caused by a too small number of averages, qubit decay (time scale of T_1) or by some instability in the measurement setup. Single and two-qubit (correlated) phase errors, correspond to a partial or full swap of elements with X and Y preparation and measurement. When phase-sensitive measurements of X and Y components are both dim when a superposition was prepared, it marks qubit dephasing (time scale of T_2). Comparison of the different columns shows if the error corresponds to a single qubit, to both qubits independently, or if only the states of the two-excitation manifold show an error. For example it would reveal, which out of the three flux pulse buffers described in Section 2.4 and 2.5 is miscalibrated. As in the io-map representation all relevant errors are easy to distinguish and it is composed of measurement data without more complicated algebra, it is helpful for debugging the experiments.

By substituting U_{bare} in place of U_{ideal} in Equation 3.10, the flux pulse length and amplitude errors can be simulated. With a help of modern mathematics software like *Wolfram Mathematica* it is easy to systematically study the derivatives of elements of the io-map. Partial derivatives by flux pulse amplitude θ and length t

$$\left.\frac{\partial\langle M\rangle_{kl}}{\partial\theta}\right|_{\substack{\theta_{i\text{-SWAP}}\\ t_{i\text{-SWAP}}}} \text{ and } \left.\frac{\partial\langle M\rangle_{kl}}{\partial t}\right|_{\substack{\theta_{i\text{-SWAP}}\\ t_{i\text{-SWAP}}}} \tag{3.11}$$

respectively at optimal configuration are shown in Figure 17. It reveals, that some elements are more sensitive to miscalibration. It also confirms, that as discussed before in Section 2.1 the Chevron pattern measurement, corresponding to preparation Z_+Z_- and readout Z_-Z_+, is first-order insensitive to both of the errors. A similar method can be used to learn about the sensitivity to errors of other parameters like buffer amplitudes.

Comparison of partial derivatives reveals preparation and readout combinations most sensitive to one kind of errors and insensitive to the other. For example the measurement of Y_-Z_+ and preparation of X_+Z_- gives a θ *error syndrome* insensitive to errors in t, qubit A phase errors before and after the two-qubit operations or the two-qubit correlated phase error denoted with $(\theta|X_+Z_-|Y_-Z_+)$. Thus the syndrome enables a first-order sensitive flux pulse amplitude fine tuning, when already close to the optimal configuration. A similar t error syndrome $(t|Y_+Z_-|Y_-Z_+)$ corresponds to the same measurement, but to the preparation of Y_+Z_-. The corresponding landscapes of the expectation value $\langle M\rangle$ as function of t and θ are shown in Figure 18. For these syndromes the optimal $\langle M\rangle$ corresponds to $m_{eg} = 0.6$ which we fixed for the study. Both of the syndromes are nearly linear around the optimal i-SWAP configuration. Some other method can be used to get the initial guess value inside the fidelity contour of 80 % where the syndrome measurement at few configurations reveals the optimal

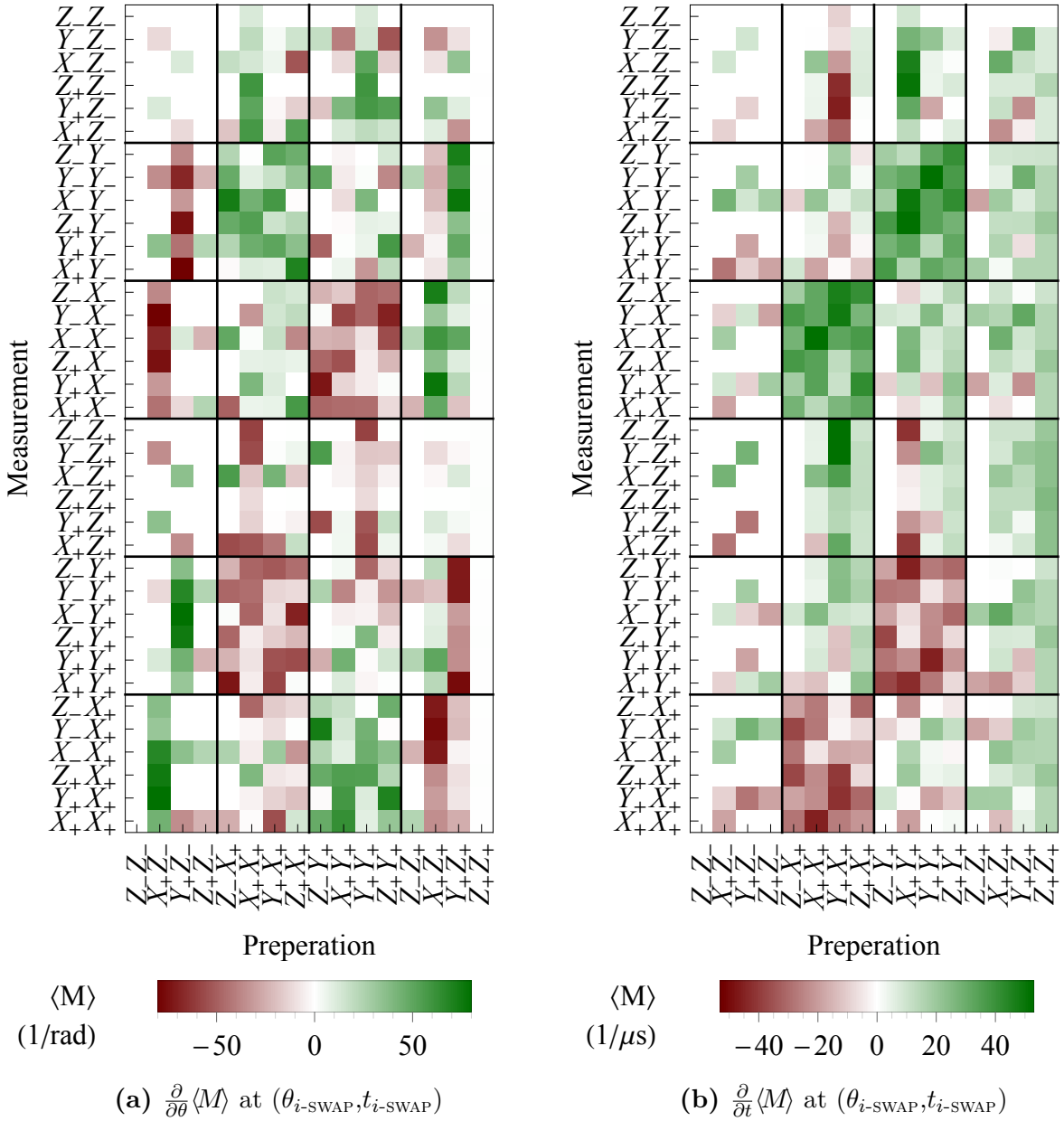

(a) $\frac{\partial}{\partial\theta}\langle M\rangle$ at $(\theta_{i\text{-SWAP}}, t_{i\text{-SWAP}})$ **(b)** $\frac{\partial}{\partial t}\langle M\rangle$ at $(\theta_{i\text{-SWAP}}, t_{i\text{-SWAP}})$

Figure 17: Derivatives of theoretical io-map for the i-SWAP gate implementation. Axes labels are same as in Figure 16. Colours represent the derivative of $\langle M\rangle$ with respect to flux pulse amplitude θ and length t.

gate parameters.

At this point described syndrome measurements are not needed in the experiment, as the method described in Section 2.1 efficiently converges to the limit set by the AWG time and amplitude resolution. The next-generation chips on the other hand will probably have smaller coupling strengths g making also J smaller. This makes the gate slower increasing the effective AWG resolution. Similarly smaller J allows qubit parking closer to two qubit operation bias points thus increasing the effective AWG amplitude resolution. In this case it is possible, that a first-order insensitive objective function, like the Chevron patter, becomes inefficient and the described or other error syndromes found by the io-map representation will help to achieve high-fidelity multi-qubit gates.

3.4 Pauli transfer matrix

Closely related to io-map is the standard representation referred to as *Pauli transfer matrix* [Chow 12]. Quantum state tomography fully describes the output states and if the input states span the whole two-qubit state space, it is possible to map the input state components to output state components. In case of the Pauli transfer matrix the qubit state basis is fixed to Pauli matrices $\sigma_i \in \{\mathbb{1}, \sigma_x, \sigma_y, \sigma_z\}$ and the map $\mathcal{R}$ fixes the input-output relation

$$p^{out} = \mathcal{R}\, p^{in} \tag{3.12}$$

of Pauli state vectors. The two-qubit Pauli state vector for the input state ρ_k is

$$p^{in}_{kl} = \mathrm{Tr}[\rho_k(\sigma_i \otimes \sigma_j)_l]\,, \tag{3.13}$$

where $i, j \in [1 \ldots 4]$ and $k, l \in [1 \ldots 16]$. Similar definitions hold for p^{out} or the coefficients r directly from the quantum state tomography (Equation 3.5) can be used. This makes it straight forward to compose Pauli transfer matrix from the data already available. Solving the input-output relation given in Equation 3.12 gives

$$\mathcal{R}_{kl} = \sum_{n}^{16} p^{in}_{nk}\, p^{out}_{nl} \tag{3.14}$$

where the order of indexes in matrix product was changed instead of transposing p^{in}. Examples of Pauli transfer matrix of ideal and measured $\mathbb{1}$ and i-SWAP gates are shown in Figure 19. Average gate fidelities are 83.7 % for data set `good-`$\mathbb{1}$ and 81.6 % for data set `good-`i-SWAP. Unlike in the case of io-map or process matrix described in the next section, the Pauli transfer matrix has a fixed basis. In addition the matrix components are always real due to the choice of the basis and therefore there is no need to separately plot the imaginary parts.

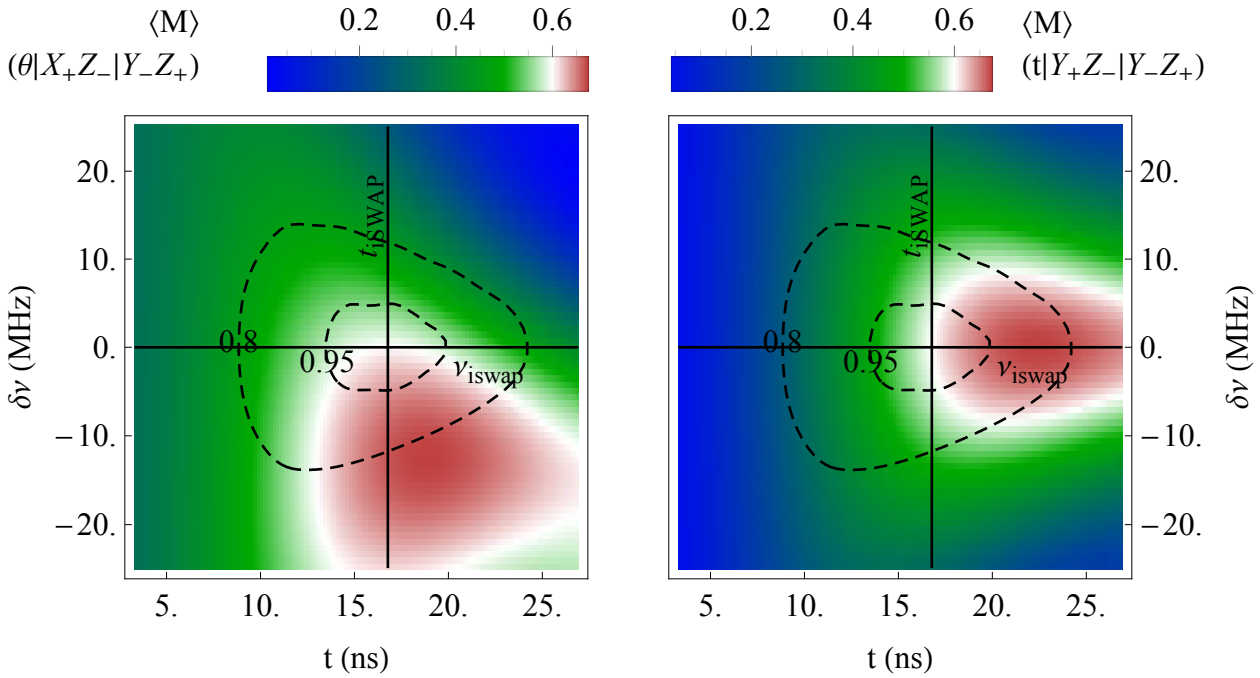

(a) Amplitude error syndrome landscape.

(b) Length error syndrome landscape.

Figure 18: Two simulated error syndromes - measurements sensitive to only one type of the flux pulse error. Colours represent the measurement value as function of the detuning from resonance $\delta\nu$ and the length of the interaction t. The optimal ν and t values are marked with the solid grid lines. Optimal measurement value is represented with white. Contours corresponding to the fidelity values 0.8 and 0.95 are marked with dashed lines. Both of the syndromes are first-order sensitive.

If the studied operation is of the Clifford group[16], the non-zero matrix elements are all ± 1. On the other hand arbitrary phase errors, dephasing and decay are harder to distinguish than in case of io-map. The Pauli transfer matrix was presented and discussed in more detail in [Chow 12].

3.5 Process matrix representation

The best known description of a process in an open quantum system, is so called χ or *process matrix representation* [Nielsen 00, Ch. 8] which describes the completely positive linear map

[16]Normaliser of the Pauli group - all operations which do not take states out of set of eigenstates of the Pauli operators [Córcoles 13].

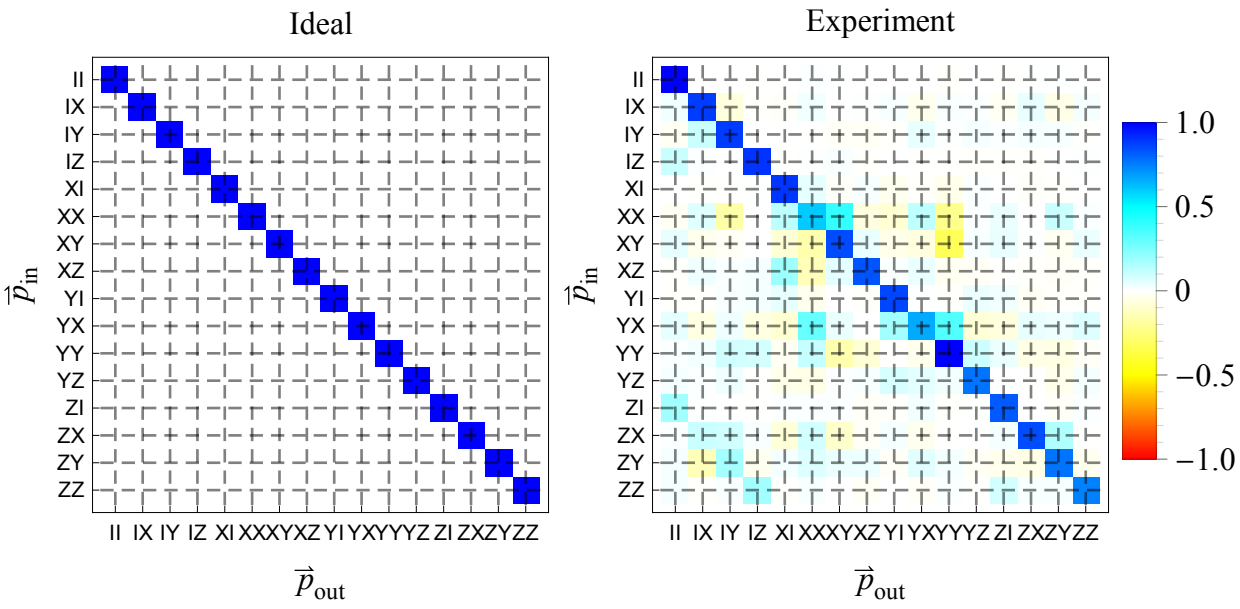

(a) Identity process

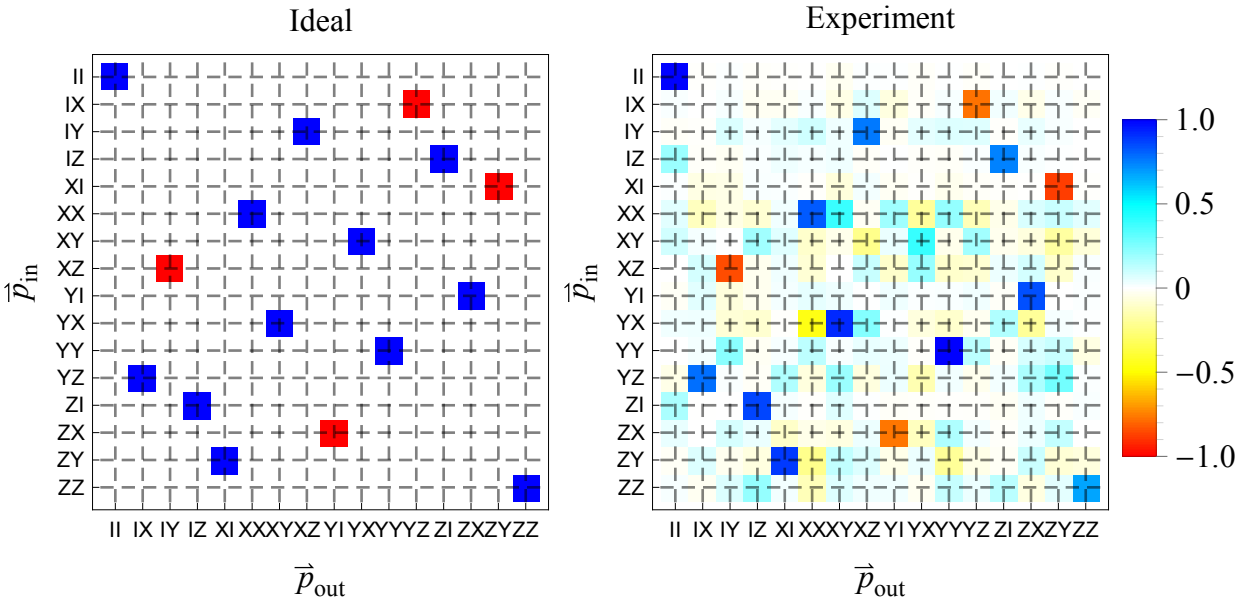

(b) i-SWAP process

Figure 19: Pauli transfer map matrices of ideal gates and experimental data sets `good-`$\mathbb{1}$ and `good-`i-SWAP. The tick labels mark the Pauli vector components for the basis $\{\mathbb{1}, \sigma_x, \sigma_y, \sigma_z\} = \{\mathsf{I}, \mathsf{X}, \mathsf{Y}, \mathsf{Z}\}$.

$$\varepsilon(\rho) = \sum_{k,l} \chi_{kl} \, E_k \, \rho \, E_l^\dagger \tag{3.15}$$

of input state ρ in a fixed basis of operators E_k. If χ is the unit matrix the representation is equivalent to *Kraus operator sum representation* [Kraus 83]. The goal of quantum process tomography is to reconstruct χ by preparing a set of input states ρ_n and fully characterising output states $\varrho_n = \varepsilon(\rho_n)$ by quantum state tomography. The only necessary assumption about the experiment requires that the state preparation shares no significant entanglement with the state manipulator nor with the measurement device [Chuang 97]. In our case this requirement is fulfilled by having low enough thermal excitation probability and pulsed measurement[17].

The task is again described by a set of linear equation

$$\lambda_{nm} = \sum_{kl} \beta_{nm}^{kl} \chi_{kl} \tag{3.16}$$

where

$$\lambda_{nm} = \mathrm{Tr}\left[\varrho_n b_m^\dagger\right] \tag{3.17}$$

describes the measurement results in some orthogonal[18] density matrix basis $\{b_m\}$ and a $4D$ tensor

$$\beta_{nm}^{kl} = \mathrm{Tr}\left[E_m \rho_k E_n^\dagger b_l^\dagger\right] \tag{3.18}$$

maps the experiment data to the chosen operator basis taking the density matrix basis into account. In case of two qubit process tomography the indices are $k, l, n, m \in [1 \ldots 16]$. The Equation 3.16 can be solved by inverting β using some standard software like *Wolfram Mathematica*. For a detailed discussion of the formalism see [Chuang 97].

If the density matrix basis b_m is chosen to be the set of expected output states $\varrho_n = U_{ideal} \rho_n U_{ideal}^\dagger$, the matrix λ_{nm} provides some information for debugging. An over-complete set of preparation states ρ may be used to suppress the systematic errors as also discussed in Section 3.1.

The optimal choice for operator basis E_m varies depending on application. It is common to show processes in the basis of Pauli operators which in case of the two qubits is given by

$$E_m = (\tilde{\sigma}_i \otimes \tilde{\sigma}_j)_m \tag{3.19}$$

[17] The transmition measurement tone is switched on only for a short time compared to measurement repetition rate and any possible residual photons would decay.

[18] See derivation in [Nielsen 00, p. 391] or [Chuang 97].

where $\tilde{\sigma}_i = \tilde{\sigma}_j = \{\sigma_0, \sigma_x, -i\sigma_y, \sigma_z\}$ with σ_y multiplied by $-i$ to make E real for real coefficients. Such representation of experimental data set `good-`i-SWAP and theoretical i-SWAP gate is shown in Figure 20.

The averaged process fidelity of a processes described by χ_{exp} related to the ideal process χ_{ideal} is given by [Steffen 13b]

$$F = \mathrm{Tr}[\chi_{exp}\chi_{ideal}] \tag{3.20}$$

and all process fidelities in the thesis are given by this relation.

3.6 Phase degree of freedom

The process matrix representation is useful for finding errors related to the operator basis $\{E_m\}$. In the Sections 2.4 and 2.5 different gate phase component calibrations were described. As the single and two qubit phase gates correspond to the action of $\mathbb{1} \otimes \sigma_z, \sigma_z \otimes \mathbb{1}$ and $\sigma_z \otimes \sigma_z$, all elements of $\tilde{\sigma}$, the phase errors effect single matrix elements. In contrast the decay and dephasing of the qubits are expressed by many matrix elements and are not easy to recognize in general.

In case of $\mathbb{1}$ process with global phase left free, there are 3 relevant phases: two single qubit phases $\phi_{A,B}$ of states $|01\rangle$ and $|10\rangle$ and *correlated* or *conditional* phase ψ of state $|11\rangle$. The phase degree of freedom can be simulated by

$$U_{\text{freePhase}} = \mathbb{1}Z(\phi_A)Z\mathbb{1}(\phi_B)ZZ(\psi) = \tag{3.21}$$

$$= \begin{pmatrix} 1 & 0 & 0 & 0 \\ 0 & e^{-i\phi_A} & 0 & 0 \\ 0 & 0 & e^{-i\phi_B} & 0 \\ 0 & 0 & 0 & e^{-i(\phi_A+\phi_B+\psi)} \end{pmatrix}. \tag{3.22}$$

By expanding the $U_{\text{freePhase}}$ in basis of $\tilde{\sigma}$ by

$$U_{\text{freePhase}} = \sum_k a_k \tilde{\sigma}_k \tag{3.23}$$

the $\chi_{kl} = a_k a_l^*$ is recovered.

By maximising the fidelity $F = \mathrm{Tr}[\chi_{\text{freePhase}}\chi_{\text{exp}}]$ as a function of phases $\phi_{A,B}$ and ψ using numeric optimization tools, we have a method for quantifying phase errors independently from the Ramsey-type of measurement described in Sections 2.4 and 2.5. Note, that unlike the methods described before, this one can be used for any gate by generalising $U_{\text{freePhase}}$.

As an example the process matrix of $\mathbb{1}$ gate in $\tilde{\sigma}$ basis are shown in Figure 21. For demonstration, the shown gate did not make use of conditional phase compensation buffer described in

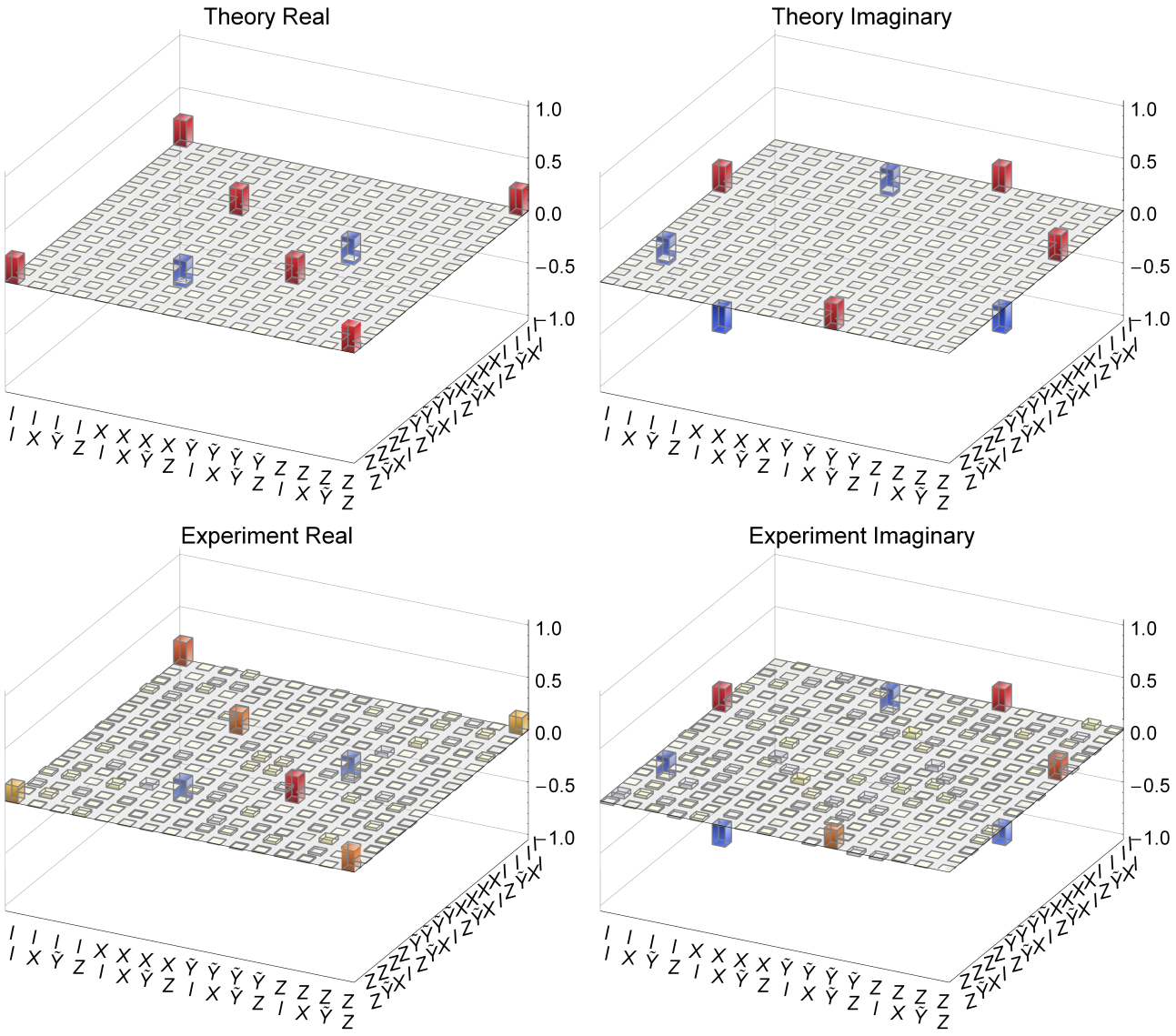

Figure 20: Process matrix representation of i-SWAP process. The top plots show the real (left) and imaginary (right) components of the ideal operations for comparison to the experimental data shown on lower plots. The tick labels mark the operator basis elements $\tilde{\sigma} = \{\sigma_0, \sigma_x, -i\sigma_y, \sigma_z\} = \left\{\mathsf{I}, \mathsf{X}, \tilde{\mathsf{Y}}, \mathsf{Z}\right\}$. The same experiment data set `good-`i-SWAP in the Pauli transfer matrix representation was shown in Figure 19.

Section 2.5 and therefore had a correlated phase error. The phases obtained by fidelity fitting show dynamic phase shifts of $\phi_a = -7°$, $\phi_b = 0°$ and $\psi = -89°$. The small single-qubit phase ϕ_a is probably due to qubit instability. The fidelity of the shown process is only 60 % related to ideal identity gate and 89 % in relation to phase fitted identity also shown in Figure 21. This emphasises once more the importance of conditional phase calibration.

3.7 Choi matrix and qubit decay

If the operator basis E of process matrix is chosen

$$E_k = C_k = |i\rangle\langle j| \, \varepsilon(|i\rangle\langle j|) = |i\rangle\langle j| \, U_{\text{ideal}} \, |i\rangle\langle j| \, U_{\text{ideal}}^{\dagger}, \tag{3.24}$$

it will directly map computational basis states of the input density matrix to elements of the output density matrix. Such process matrix representation is referred to as *Choi matrix* [Choi 75, Leung 03]. In case of two qubits indexes $i, j \in \{gg, ge, eg, ee\}$ and $k \in [1 \ldots 16]$. When phase errors were easy to recognize in $\tilde{\sigma}$ operator basis, the decay, dephasing, depolarisation and other similar errors, which influence the density matrices in a straight forward way, are easy to see in the C operator basis. For definitions of mentioned loss channels see Appendix A or [Nielsen 00, p. 397]. In order to simulate the quantum channel with several characteristic errors we first concatenate the Kraus operator sum representations by

$$\varepsilon_1(\varepsilon_2(\rho)) = \varepsilon_1\varepsilon_2(\rho) = \tag{3.25}$$

$$= \sum_i \sum_j \overline{E}_i \tilde{E}_j \rho \tilde{E}_j^{\dagger} \overline{E}_i^{\dagger} = \tag{3.26}$$

$$= \sum_{i,j} E_{i,j} \rho E_{i,j}^{\dagger}. \tag{3.27}$$

In addition to the qubit decay channel $\varepsilon_{\text{decay}}$ and dephasing channel $\varepsilon_{\text{dephase}}$, the depolarising channel $\varepsilon_{\text{depol}}$ was studied, as depolarisation would correspond to random qubit control errors. Once again software assistance is necessary, as the concatenated error channel $\varepsilon_{\text{decay}}\varepsilon_{\text{dephase}}\varepsilon_{\text{depol}}(\cdot)$ consists of 141 unique operator elements in case of two qubits. The comparison of Choi matrices of the measured $\mathbb{1}$ gate and the process which we expect solely from decay and dephasing of the qubits, are shown in Figure 22. The Choi plot of simulated decay channel uses fluxed qubit A and target qubit B lifetimes $\mathrm{T}_1 = \{1.8\,\mu\text{s}, 2.6\,\mu\text{s}\}$ and $\mathrm{T}_2 = \{1.8\,\mu\text{s}, 3.4\,\mu\text{s}\}$ respectively. They were obtained from the last calibration routine[19] before the process tomography.

The fidelity of the estimated decay channel for the given qubit lifetimes in relation to the ideal identity gate is 87.6 % in comparison to 83.7 % for the dataset shown. From Figure 22 it

[19] For details on single-qubit calibration routines, including T_1 ant T_2 measurements, see [Baur 12, Ch. 5].

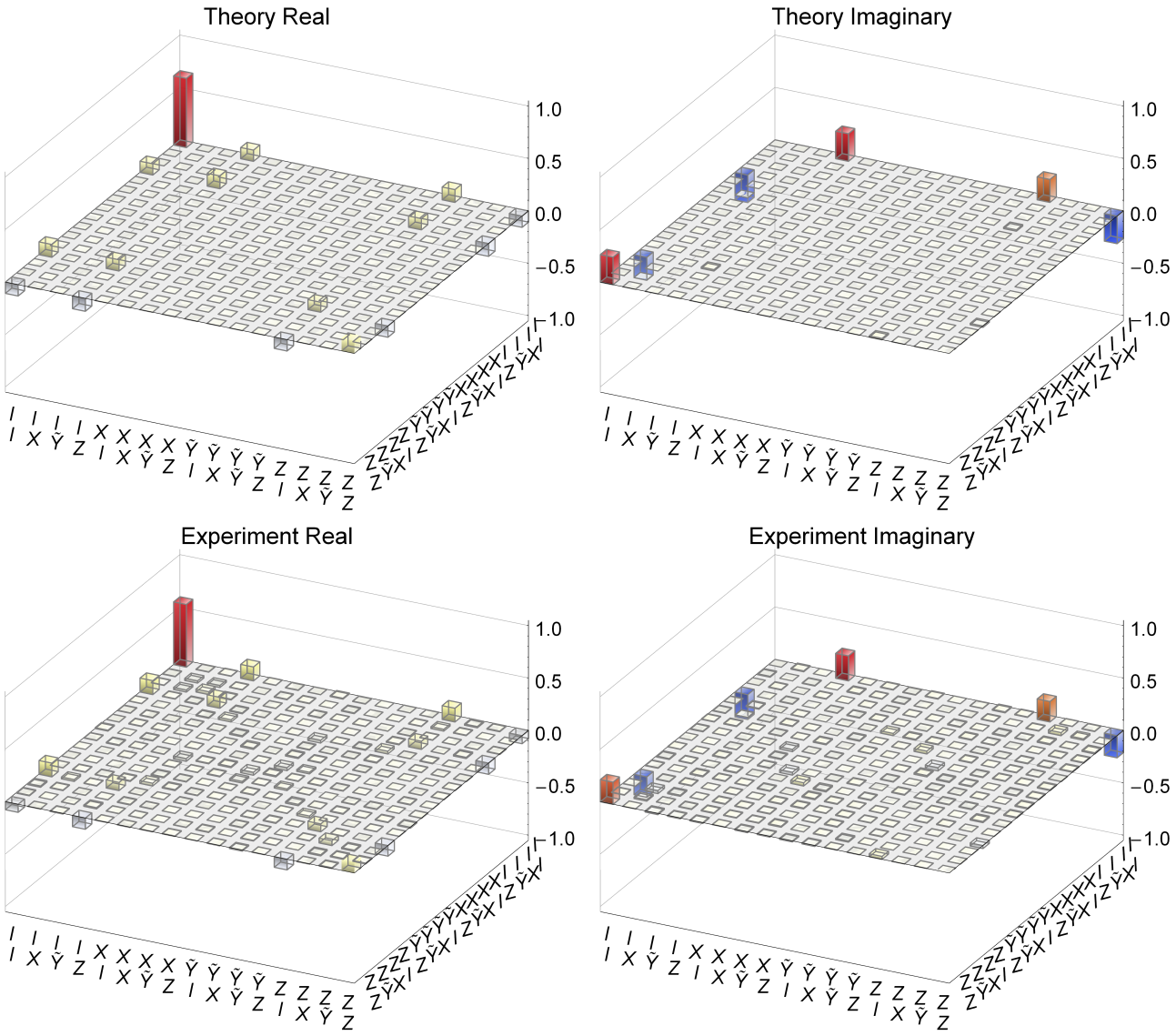

Figure 21: Process matrix representation of $\mathbb{1}$ process without conditional phase compensation buffer. The top plots show the real (left) and imaginary (right) components of theoretical $U_{\text{freePhase}}$ closest to the experiment data set `bad-`$\mathbb{1}$ shown on lower plots. For corresponding process fidelities and phase shifts of theoretical process see main text. The tick labels are the same as in Figure 20.

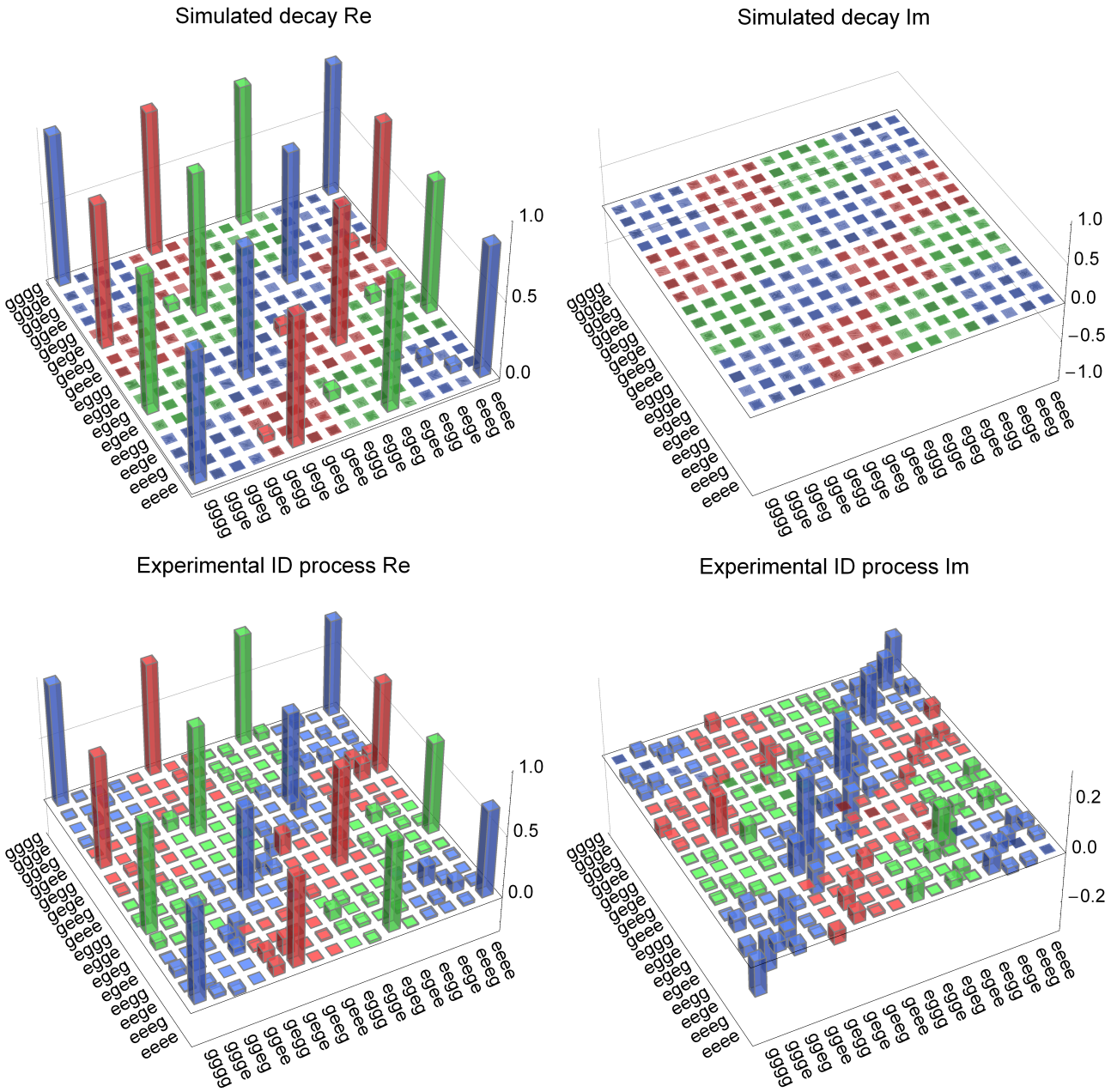

Figure 22: Theoretical decay process (top) in Choi matrix representation real and imaginary parts (left and right) in comparison to the experimental data `good-1` (bottom). Sub-matrices corresponding to different computational input states are coloured differently to improve readability. The same experiment data set in the Pauli transfer matrix representation was shown in Figure 19.

can also be seen, that decay alone does not completely describe the process. For the specific data set few percent further improvement seems possible from studding the phase errors in process tomography, but this would not explain the whole fidelity loss.
It was already discussed in Section 2.3, that there are problems with medium time scale qubit fluctuations, which are too fast for calibration measurements, and two slow to be studied in conventional measurements. This needs further study. Due to this, or due to some other reason there are systematic state preparation and measurement (SPaM) errors. In order to suppress them, over-complete state and process tomography could be tried. Qubit dephasing and decay time are steadily improving and importance of exact control and error diagnostic are of increasing value. The process matrix has proven to be another useful tool in quantum mechanics toolbox.

Summary

Modular multi-qubit gate design was pursued, which enables concatenation of once calibrated gates. This required study of the time dynamics of the qubit detuning with various delayed Ramsey type of measurements. We found, that flux pulse induced screening current can be compensated with an amplitude-inverted copy of the first pulse. This enables us to consider the next operation independent from the previous 75 ns after the flux pulse.
For the daily recalibration automatic routines were implemented. To quickly find the optimal flux pulse amplitude and length a Nelder-Mead derivative-free optimization method is used. Then the dynamic phase the fluxed qubit collects when taken from one rotating reference frame to another in the beginning and end of the gate, is compensated using two buffers. The amplitudes are found by a buffer amplitude sweep and fit of a simple theoretical model. In addition a method was developed to compensate the conditional phase the qubits collect due to the finite qubit-qubit coupling even at the parking position by using an additional buffer, which implements a CARB-PHASE gate. This is done even for a finite-length two-qubit identity gate to improve its fidelity.
To study the details of the implemented gates several different representations of quantum processes were investigated and implemented for future reuse. The input-output-map was developed to provide useful information for experimentalists. It also provides a method to find significant non-trivial error syndromes. In addition the Pauli transfer matrix and processes matrix in Pauli operator and Choi basis were implemented, compared and documented. Finally the implemented two-qubit process tomography gave a fidelity of the i-SWAP and identity processes over 81 %. As the theoretical qubit lifetime limited fidelity is around 86 % there is still room for improvement. Several suggestions were made throughout the discussion.

Acknowledgements

The developed software and analysis of the quantum state and process tomography rely heavily on the code libraries developed in the lab before by William Zeng, Dr. Stefan Filipp and many other.

I am very grateful to Prof. Andreas Wallraff for many opportunities I have had in the lab. Warmest thanks I owe to Yves Salathé for the active collaboration and kind guidance in all aspects of scientific work. I would also like to thank Dr. Mintu Mondal for the tutoring regarding the experiments and all members of the Qudev group for creating a friendly and pleasant atmosphere.

My studies in ETH Physics master program would not have been possible, if there had not been the financial aid by the Kristjan Jaak scholarship program, Estonian Student Fund in USA and Harald Raudsep' scholarship from Estonian-Revelia Academic Fund.

A Notation

Qubit states are easily visualised in the Bloch sphere representation, as shown in Figure 23. It is analogous to the Poincaré sphere from polarisation optics or to the state space of a spin $\frac{1}{2}$ particle. In this representation, the qubit state correspond to a point in or on the sphere corresponding to mixed or pure states accordingly.

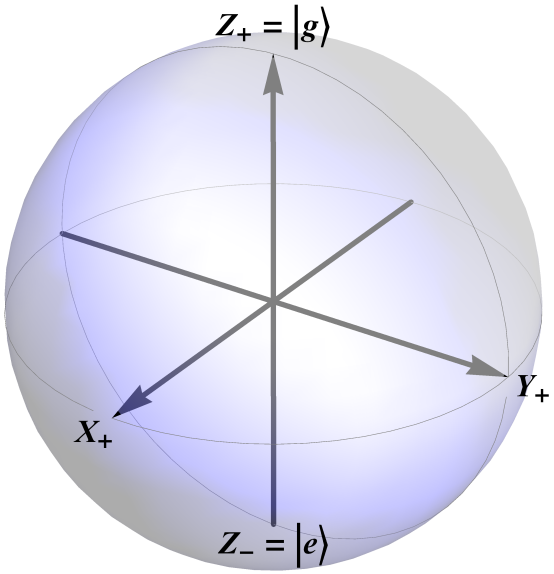

Figure 23: Bloch sphere with axes labels standing for the eigenstates of the Pauli operators corresponding to the positive and negative eigenvalues.

In the Bloch sphere the coordinates of the state with a density matrix ρ are spanned by the Pauli operators σ_i by

$$\rho = \tfrac{1}{4}\left(p_0\mathbb{1} + p_1\sigma_x + p_2\sigma_y + p_3\sigma_z\right) \tag{A.1}$$

where vector p_i is referred to as Pauli state vector. This is analogues to the Stokes vector in polarisation optics.

The initial states of experiments and simulations is taken to be the ground state of both qubits

$$|gg\rangle = \begin{pmatrix}1\\0\\0\end{pmatrix}_A \otimes \begin{pmatrix}1\\0\\0\end{pmatrix}_B . \tag{A.2}$$

which is manipulated using generalized Pauli operators for three level systems corresponding

to the MW pulses done in the experiment:

$$\sigma_0^{3l} = \begin{pmatrix} 1 & 0 & 0 \\ 0 & 1 & 0 \\ 0 & 0 & 1 \end{pmatrix}; \sigma_x^{3l} = \begin{pmatrix} 0 & 1 & 0 \\ 1 & 0 & 0 \\ 0 & 0 & 1 \end{pmatrix}; \sigma_y^{3l} = \begin{pmatrix} 0 & -i & 0 \\ i & 0 & 0 \\ 0 & 0 & 1 \end{pmatrix}; \sigma_z^{3l} = \begin{pmatrix} 1 & 0 & 0 \\ 0 & -1 & 0 \\ 0 & 0 & 1 \end{pmatrix}. \tag{A.3}$$

Note, that the label eigenstate corresponds to the positive eigenvalue of σ_z as a ground state, which is one of the degenerate eigenstates of σ_z^{3l}. If it is clear from the dimensions, which one is used I will drop the ^{3l} tag. Corresponding ϕ rotation operators are

$$\mathbb{1}(\phi) = e^{(-i\phi/2\sigma_0)}; X(\phi) = e^{(-i\phi/2\sigma_x)}; Y(\phi) = e^{(-i\phi/2\sigma_y)}; Z(\phi) = e^{(-i\phi/2\sigma_z)}. \tag{A.4}$$

Similarly two-qubit rotation operators can be built. For example

$$\mathbb{1}Z(\phi) = e^{(-i\phi/2(\sigma_0 \otimes \sigma_z))}; ZZ(\phi) = e^{(-i\phi/2(\sigma_z \otimes \sigma_z))}. \tag{A.5}$$

The two-qubit gates used throughout the thesis are

$$U_{\text{SWAP}} = \begin{pmatrix} 1 & 0 & 0 & 0 \\ 0 & 0 & 1 & 0 \\ 0 & 1 & 0 & 0 \\ 0 & 0 & 0 & 1 \end{pmatrix}, \tag{A.6a}$$

$$U_{i\text{-SWAP}} = \begin{pmatrix} 1 & 0 & 0 & 0 \\ 0 & 0 & i & 0 \\ 0 & i & 0 & 0 \\ 0 & 0 & 0 & 1 \end{pmatrix}, \tag{A.6b}$$

$$U_{\text{c-PHASE}} = \begin{pmatrix} 1 & 0 & 0 & 0 \\ 0 & 1 & 0 & 0 \\ 0 & 0 & 1 & 0 \\ 0 & 0 & 0 & -1 \end{pmatrix}, \tag{A.6c}$$

$$U_{\text{CARB-PHASE}} = \begin{pmatrix} 1 & 0 & 0 & 0 \\ 0 & 1 & 0 & 0 \\ 0 & 0 & 1 & 0 \\ 0 & 0 & 0 & e^{-i\phi} \end{pmatrix}, \tag{A.6d}$$

$$U_{dyn}(\phi_A, \phi_B) = \begin{pmatrix} 1 & 0 & 0 & 0 \\ 0 & e^{-i\phi_A} & 0 & 0 \\ 0 & 0 & e^{-i\phi_B} & 0 \\ 0 & 0 & 0 & 1 \end{pmatrix}. \tag{A.6e}$$

The qubit decay, dephasing and depolarisation processes are described by following operator sum elements [Nielsen 00, p. 397]

$$E_{decay} = \left\{ \begin{pmatrix} 1 & 0 \\ 0 & \sqrt{1-\gamma} \end{pmatrix}, \begin{pmatrix} 0 & \sqrt{\gamma} \\ 0 & 0 \end{pmatrix} \right\}; \tag{A.7a}$$

$$E_{dephase} = \left\{ \begin{pmatrix} 1 & 0 \\ 0 & \sqrt{1-\gamma} \end{pmatrix}, \begin{pmatrix} 0 & 0 \\ 0 & \sqrt{\gamma} \end{pmatrix} \right\}; \tag{A.7b}$$

$$E_{depol} = \left\{ \sqrt{1-\frac{3p}{4}}\sigma_0, \sqrt{\frac{p}{4}}\sigma_x, \sqrt{\frac{p}{4}}\sigma_y, \sqrt{\frac{p}{4}}\sigma_z \right\}. \tag{A.7c}$$

B Data set details

For comparison with future experiments the details about presented data sets are provided in Table 2. Qubit decay time T_1 and dephasing time T_2 for both of the qubits were measured in separate measurement as a part of standard calibration routines. The full process tomography provides the process fidelity and it was compared to the fidelity, which would correspond to the experiment data, if the single and two qubit phase errors had been intended and to the theoretically obtained maximal fidelity for given qubit lifetimes. For information, on how these fidelities were obtained, see Sections 3.5, 3.6 and 3.7 correspondingly.

Data set reference	`bad-𝟙`	`good-𝟙`	`good-`i-SWAP
Data set id	`140605-1111`	`140621-1204`	`140627-2263`
T_1 of Qb A, B (μs)	1.8, 2.8	1.9, 2.6	1.8, 2.5
T_2 of Qb A, B (μs)	1.7, 4.0	1.8, 3.4	1.7, 3.9
Gate length (ns)	218.7	198.0	245.5
Fidelity of experiment data	41.3 %	83.7 %	81.6 %
Fidelity without phase error	89.2 %	83.8 %	82.0 %
Lifetime limit for fidelity	88.0 %	87.6 %	86.2 %

Table 2: Detailed information about the three data sets discussed in the thesis.

Note, that for dataset `bad-𝟙` the estimated phase-errorless fidelity is larger than the limit set by qubit lifetime. This apparent contradiction is probably due to the method being too optimistic as it could compensate a part of dephasing to be a phase error.

References

[Aspect 82] Alain Aspect, Jean Dalibard & Gérard Roger. *Experimental Test of Bell's Inequalities Using Time- Varying Analyzers*. Phys. Rev. Lett., vol. 49, no. 25, pages 1804–1807, Dec 1982. 5

[Baldwin 14] C. H. Baldwin, A. Kalev & I. H. Deutsch. *Quantum process tomography of unitary and near-unitary maps*. ArXiv e-prints, April 2014. 32

[Barends 14] R. Barends, J. Kelly, A. Megrant, A. Veitia, D. Sank, E. Jeffrey, T. C. White, J. Mutus, A. G. Fowler, B. Campbell, Y. Chen, Z. Chen, B. Chiaro, A. Dunsworth, C. Neill, P. OMalley, P. Roushan, A. Vainsencher, J. Wenner, A. N. Korotkov, A. N. Cleland & John M. Martinis. *Superconducting quantum circuits at the surface code threshold for fault tolerance*. Nature, vol. 508, no. 7497, pages 500–503, April 2014. 5, 16, 23, 24

[Baur 12] M. Baur, A. Wallraff & D. Vion. Realizing quantum gates and algorithms with three superconducting qubits. ETH, 2012. 7, 10, 14, 15, 16, 21, 24, 25, 47

[Blais 04] A. Blais, R.-S. Huang, A. Wallraff, S. M. Girvin & R. J. Schoelkopf. *Cavity quantum electrodynamics for superconducting electrical circuits: An architecture for quantum computation*. Phys. Rev. A, vol. 69, no. 6, pages 062320–14, June 2004. 8, 12, 33

[Blais 07] A. Blais, J. Gambetta, A. Wallraff, D. I. Schuster, S. M. Girvin, M. H. Devoret & R. J. Schoelkopf. *Quantum-information processing with circuit quantum electrodynamics*. Phys. Rev. A, vol. 75, no. 3, pages 032329–21, March 2007. 5, 8, 9

[Bouchiat 98] V. Bouchiat, D. Vion, P. Joyez, D. Esteve & M. H. Devoret. *Quantum coherence with a single Cooper pair*. Phys. Scr., vol. T76, pages 165–170, 1998. 6

[Bozyigit 10] Deniz Bozyigit. Correlation function measurements of a microwave frequency single photon source. Master's thesis, ETH Zurich, 04 2010. 24

[Bremner 02] Michael J. Bremner, Christopher M. Dawson, Jennifer L. Dodd, Alexei Gilchrist, Aram W. Harrow, Duncan Mortimer, Michael A. Nielsen & Tobias J. Osborne. *Practical Scheme for Quantum Computation with Any Two-Qubit Entangling Gate*. Phys. Rev. Lett., vol. 89, page 247902, Nov 2002. 9

[Brylinski 02] Ranee K Brylinski & Goong Chen. Mathematics of quantum computation. CRC Press, 2002. 9

[Büttiker 87] M. Büttiker. *Zero-current persistent potential drop across small-capacitance Josephson junctions*. Phys. Rev. B, vol. 36, no. 7, pages 3548–3555, Sep 1987. 5

[Cheney 12] E. Cheney & D. Kincaid. Numerical mathematics and computing. Cengage Learning, 2012. 35

[Childress 13] Lilian Childress & Ronald Hanson. *Diamond NV centers for quantum computing and quantum networks*. MRS Bulletin, vol. 38, pages 134–138, 2 2013. 5

[Choi 75] Man-Duen Choi. *Completely positive linear maps on complex matrices*. Linear Algebra Appl., vol. 10, no. 3, pages 285 – 290, 1975. 47

[Chow 12] Jerry M. Chow, Jay M. Gambetta, A. D. Córcoles, Seth T. Merkel, John A. Smolin, Chad Rigetti, S. Poletto, George A. Keefe, Mary B. Rothwell, J. R. Rozen, Mark B. Ketchen & M. Steffen. *Universal Quantum Gate Set Approaching Fault-Tolerant Thresholds with Superconducting Qubits*. Phys. Rev. Lett., vol. 109, page 060501, Aug 2012. 41, 42

[Chuang 97] Isaac L. Chuang & M. A. Nielsen. *Prescription for experimental determination of the dynamics of a quantum black box*. J. Mod. Opt., vol. 44, no. 11, pages 2455–2467, 1997. 32, 44

[Chuang 98] Isaac L. Chuang, Lieven M. K. Vandersypen, Xinlan Zhou, Debbie W. Leung & Seth Lloyd. *Experimental realization of a quantum algorithm*. Nature, vol. 393, no. 6681, pages 143–146, May 1998. 5

[Clarke 08] John Clarke & Frank K. Wilhelm. *Superconducting quantum bits*. Nature, vol. 453, no. 7198, pages 1031–1042, June 2008. 5

[Cohen-Tannoudji 89] Claude Cohen-Tannoudji, Jacques Dupont-Roc & Gilbert Grynberg. Photons & atoms - introduction to quantum electrodynamics. Wiley, 1989. 5

[Córcoles 13] A. D. Córcoles, Jay M. Gambetta, Jerry M. Chow, John A. Smolin, Matthew Ware, Joel Strand, B. L. T. Plourde & M. Steffen. *Process verification of two-qubit quantum gates by randomized benchmarking*. Phys. Rev. A, vol. 87, no. 3, Mar 2013. 16, 42

[Cottet 02] A. Cottet. *Implementation of a quantum bit in a superconducting circuit*. PhD thesis, Université Paris 6, 2002. 6

[Egger 14a] D. J. Egger & F. K. Wilhelm. *Optimized controlled Z gates for two superconducting qubits coupled through a resonator*. Superconductor Science and Technology, vol. 27, page 014001, 2014. 31

[Egger 14b] J. Egger D. & K. Wilhelm F.˙ *Adaptive Hybrid Optimal Quantum Control for Imprecisely Characterized Systems*. Phys. Rev. Lett., vol. 112, page 240503, Jun 2014. 31

[Eichler 14] C. Eichler, Y. Salathe, J. Mlynek, S. Schmidt & A. Wallraff. *Quantum limited amplification and entanglement in coupled nonlinear resonators*. arXiv:1404.4643, 2014. 12

[Filipp 09] S. Filipp, P. Maurer, P. J. Leek, M. Baur, R. Bianchetti, J. M. Fink, M. Göppl, L. Steffen, J. M. Gambetta, A. Blais & A. Wallraff. *Two-Qubit State Tomography Using a Joint Dispersive Readout*. Phys. Rev. Lett., vol. 102, no. 20, pages 200402–4, 2009. 5, 13, 33

[Filipp 11] S. Filipp, M. Göppl, J. M. Fink, M. Baur, R. Bianchetti, L. Steffen & A. Wallraff. *Multimode mediated qubit-qubit coupling and dark-state symmetries in circuit quantum electrodynamics*. Phys. Rev. A, vol. 83, no. 6, page 063827, Jun 2011. 8

[Fragner 08] A. Fragner, M. Göppl, J. M. Fink, M. Baur, R. Bianchetti, P. J. Leek, A. Blais & A. Wallraff. *Resolving Vacuum Fluctuations in an Electrical Circuit by Measuring the Lamb Shift*. Science, vol. 322, no. 5906, pages 1357–1360, 2008. 8

[Gambetta 11] J. M. Gambetta, F. Motzoi, S. T. Merkel & F. K. Wilhelm. *Analytic control methods for high-fidelity unitary operations in a weakly nonlinear oscillator*. Phys. Rev. A, vol. 83, no. 1, pages 012308–13, January 2011. 7

[Gershenfeld 97] N. Gershenfeld & I. Chuang. *Bulk Spin Resonance Quantum Computation*. Science, vol. 275, pages 350–356, 1997. 5

[Ghosh 13] Joydip Ghosh, Andrei Galiautdinov, Zhongyuan Zhou, Alexander N. Korotkov, John M. Martinis & Michael R. Geller. *High-fidelity controlled-σ^Z gate for resonator-based superconducting quantum computers*. Phys. Rev. A, vol. 87, page 022309, Feb 2013. 11, 24, 30

[Haffner 08] H. Haffner, C. Roos & R. Blatt. *Quantum computing with trapped ions*. Physics Reports, vol. 469, no. 4, pages 155–203, December 2008. 5

[Hanson 08] Ronald Hanson & David D. Awschalom. *Coherent manipulation of single spins in semiconductors*. Nature, vol. 453, no. 7198, pages 1043–1049, June 2008. 5

[Heinsoo 13] Johannes Heinsoo. *Automatic Multi-Qubit Gate Calibration*. Semseter thesis, ETH Zürich, 06 2013. 16, 19

[James 01] D. F. V. James, P. G. Kwiat, W. J. Munro & A. G. White. *Measurement of qubits*. Phys. Rev. A, vol. 64, page 052312, 2001. 32

[Johnson 11] Blake Johnson. *Controlling Photons in Superconducting Electrical Circuits*. PhD thesis, Yale, 2011. 23

[Kelly 14] J. Kelly, R. Barends, B. Campbell, Y. Chen, Z. Chen, B. Chiaro, A. Dunsworth, A. G. Fowler, I.-C. Hoi, E. Jeffrey, A. Megrant, J. Mutus, C. Neill, P. J. J. O'Malley, C. Quintana, P. Roushan, D. Sank, A. Vainsencher, J. Wenner, T. C. White, A. N. Cleland & J. M. Martinis. *Optimal quantum control using randomized benchmarking*. arXiv:1403.0035, 2014. 17, 30

[Khaneja 05] Navin Khaneja, Timo Reiss, Cindie Kehlet, Thomas Schulte-HerbrÃ¼ggen & Steffen J. Glaser. *Optimal control of coupled spin*

dynamics: design of {NMR} pulse sequences by gradient ascent algorithms. Journal of Magnetic Resonance, vol. 172, no. 2, pages 296 – 305, 2005. 31

[Koch 07] Jens Koch, Terri M. Yu, Jay Gambetta, A. A. Houck, D. I. Schuster, J. Majer, Alexandre Blais, M. H. Devoret, S. M. Girvin & R. J. Schoelkopf. *Charge-insensitive qubit design derived from the Cooper pair box*. Phys. Rev. A, vol. 76, no. 4, page 042319, 2007. 6, 8

[Kraus 83] Karl Kraus, Arno Bohm, John D. Dollard & W. H. Wootters. States, effects, and operations : fundamental notions of quantum theory : lectures in mathematical physics at the university of texas at austin / karl kraus ; edited by a. bohm, j.d. dollard, and w.h. wootters. Springer-Verlag Berlin ; New York, 1983. 44

[Landig 13] Andreas Landig. *Software for arbitrary single qubit and qutrit gate calibration*. Semseter thesis, ETH Zürich, August 2013. 16

[Lang 13] C. Lang, D. Bozyigit, Y. Salathe, C. Eichler & A. Wallraff. *Quantum Signal Analyzer for Itinerant Microwave Radiation*. in preparation, 2013. 13

[Las Heras 14] U. Las Heras, A. Mezzacapo, L. Lamata, S. Filipp, A. Wallraff & E. Solano. *Digital Quantum Simulation of Spin Systems in Superconducting Circuits*. Phys. Rev. Lett., vol. 112, page 200501, 2014. 4, 16

[Leung 00] Debbie W. Leung, Isaac L. Chuang, Fumiko Yamaguchi & Yoshihisa Yamamoto. *Efficient implementation of coupled logic gates for quantum computation*. Phys. Rev. A, vol. 61, page 042310, Mar 2000. 26

[Leung 03] Debbie W. Leung. *Choi's proof as a recipe for quantum process tomography*. Journal of Mathematical Physics, vol. 44, no. 2, pages 528–533, 2003. 32, 47

[Liu 05] Yu-xi Liu, L. F. Wei & Franco Nori. *Tomographic measurements on superconducting qubit states*. Phys. Rev. B, vol. 72, no. 1, page 014547, Jul 2005. 32

[Loudon 00] Rodney Loudon. The quantum theory of light. Oxford U, 2000. 5

[Magesan 12] Easwar Magesan, Jay M. Gambetta, B. R. Johnson, Colm A. Ryan, Jerry M. Chow, Seth T. Merkel, Marcus P. da Silva, George A. Keefe, Mary B. Rothwell, Thomas A. Ohki, Mark B. Ketchen & M. Steffen. *Efficient Measurement of Quantum Gate Error by Interleaved Randomized Benchmarking*. Phys. Rev. Lett., vol. 109, page 080505, Aug 2012. 17

[Majer 07] J. Majer, J. M. Chow, J. M. Gambetta, J. Koch, B. R. Johnson, J. A. Schreier, L. Frunzio, D. I. Schuster, A. A. Houck, A. Wallraff, A. Blais, M. H. Devoret, S. M. Girvin & R. J. Schoelkopf. *Coupling superconducting qubits via a cavity bus*. Nature, vol. 449, no. 7161, pages 443–447, September 2007. 8

[Menicucci 02] N. C. Menicucci & Carlton M. Caves. *Local Realistic Model for the Dynamics of Bulk-Ensemble NMR Information Processing*. Physical Review Letters, vol. 88, no. 16, pages 167901+, April 2002. 5

[Menke 13] Tim Menke. Realizing a calibration program for superconducting qubits. Master's thesis, ETH Zurich, 08 2013. 16, 21, 25

[Motzoi 09] F. Motzoi, J. M. Gambetta, P. Rebentrost & F. K. Wilhelm. *Simple Pulses for Elimination of Leakage in Weakly Nonlinear Qubits*. Phys. Rev. Lett., vol. 103, no. 11, page 110501, 2009. 7

[Nakamura 99] Y. Nakamura, Y. A. Pashkin & J. S. Tsai. *Coherent control of macroscopic quantum states in a single-Cooper-pair box*. Nature, vol. 398, no. 6730, pages 786–788, April 1999. 5

[Nielsen 00] Michael A. Nielsen & Isaac L. Chuang. Quantum computation and quantum information. Cambridge University Press, 2000. 3, 4, 5, 8, 26, 42, 44, 47, 54

[Oppliger 12] Markus Oppliger. Tomographic reconstruction of dark states in circuit quantum electrodynamcis. Master's thesis, ETH Zurich, 01 2012. 21, 22

[Pedersen 08] Line Hjortshoj Pedersen, Niels Martin Moller & Klaus Molmer. *The distribution of quantum fidelities*. Physics Letters A, vol. 372, no. 47, pages 7028 – 7032, 2008. 17

[Reed 12] M. D. Reed, L. DiCarlo, S. E. Nigg, L. Sun, L. Frunzio, S. M. Girvin & R. J. Schoelkopf. *Realization of three-qubit quantum error correction with superconducting circuits.* Nature, vol. 482, pages 382–385, February 2012. 5

[Saira 13] O.-P. Saira, J. P. Groen, J. Cramer, M. Meretska, G. de Lange & L. DiCarlo. *Entanglement genesis by ancilla-based parity measurement in 2D circuit QED.* arXiv:1311.5530, 2013. 22

[Santoro 06] Giuseppe E Santoro & Erio Tosatti. *Optimization using quantum mechanics: quantum annealing through adiabatic evolution.* Journal of Physics A: Mathematical and General, vol. 39, no. 36, page R393, 2006. 4

[Schuch 03] Norbert Schuch & Jens Siewert. *Natural two-qubit gate for quantum computation using the XY interaction.* Phys. Rev. A, vol. 67, page 032301, Mar 2003. 9

[Schutjens 13] R. Schutjens, F. Abu Dagga, D. J. Egger & F. K. Wilhelm. *Single-qubit gates in frequency-crowded transmon systems.* Phys. Rev. A, vol. 88, page 052330, Nov 2013. 7

[Sendelbach 08] S. Sendelbach, D. Hover, A. Kittel, M. Muck, John M. Martinis & R. McDermott. *Magnetism in SQUIDs at Millikelvin Temperatures.* Phys. Rev. Lett., vol. 100, no. 22, pages 227006–4, June 2008. 22

[Steffen 06] M. Steffen, M. Ansmann, R. C. Bialczak, N. Katz, E. Lucero, R. McDermott, M. Neeley, E. M. Weig, A. N. Cleland & J. M. Martinis. *Measurement of the entanglement of two superconducting qubits via state tomography.* Science, vol. 313, no. 5792, pages 1423–1425, September 2006. 5

[Steffen 12] L. Steffen, M. P. da Silva, A. Fedorov, M. Baur & A. Wallraff. *Experimental Monte Carlo Quantum Process Certification.* Phys. Rev. Lett., vol. 108, page 260506, Jun 2012. 31

[Steffen 13a] L. Steffen, Y. Salathe, M. Oppliger, P. Kurpiers, M. Baur, C. Lang, C. Eichler, G. Puebla-Hellmann, A. Fedorov & A. Wallraff. *Deterministic quantum teleportation with feed-forward in a solid state system.* Nature, vol. 500, pages 319–322, 2013. 5, 11, 12, 14, 37

[Steffen 13b] Lars Steffen. *Quantum Teleportation and Efficient Process Verification with Superconducting Circuits*. PhD thesis, ETH Zurich, 2013. 15, 45

[Strauch 03] Frederick W. Strauch, Philip R. Johnson, Alex J. Dragt, C. J. Lobb, J. R. Anderson & F. C. Wellstood. *Quantum Logic Gates for Coupled Superconducting Phase Qubits*. Phys. Rev. Lett., vol. 91, no. 16, page 167005, October 2003. 9

[Tinkham 96] M. Tinkham. Introduction to superconductivity. McGraw-Hill International Editions, 1996. 6

[Vesterinen 14] V. Vesterinen, O.-P. Saira, A. Bruno & L. DiCarlo. *Mitigating information leakage in a crowded spectrum of weakly anharmonic qubits*. arXiv:1405.0450, 2014. 7, 22

[Wallraff 04] A. Wallraff, D. I. Schuster, A. Blais, L. Frunzio, R.-S. Huang, J. Majer, S. Kumar, S. M. Girvin & R. J. Schoelkopf. *Strong coupling of a single photon to a superconducting qubit using circuit quantum electrodynamics*. Nature, vol. 431, pages 162–167, 2004. 5, 12

[Wallraff 07] A. Wallraff, D. I. Schuster, A. Blais, J. M. Gambetta, J. Schreier, L. Frunzio, M. H. Devoret, S. M. Girvin & R. J. Schoelkopf. *Sideband Transitions and Two-Tone Spectroscopy of a Superconducting Qubit Strongly Coupled to an On-Chip Cavity*. Phys. Rev. Lett., vol. 99, page 050501, 2007. 10

[Warren 97] Warren S. Warren. *The Usefulness of NMR Quantum Computing*. Science, vol. 277, no. 5332, pages 1688–1690, 1997. 5

[Wiesner 83] Stephen Wiesner. *Conjugate Coding*. SIGACT News, vol. 15, no. 1, pages 78–88, January 1983. 4

[Wu 13] Xiaohua Wu & Ke Xu. *Partial standard quantum process tomography*. Quantum Information Processing, vol. 12, no. 2, pages 1379–1393, 2013. 32

ETH

Eidgenössische Technische Hochschule Zürich
Swiss Federal Institute of Technology Zurich

Declaration of originality

The signed declaration of originality is a component of every semester paper, Bachelor's thesis, Master's thesis and any other degree paper undertaken during the course of studies, including the respective electronic versions.

Lecturers may also require a declaration of originality for other written papers compiled for their courses.

I hereby confirm that I am the sole author of the written work here enclosed and that I have compiled it in my own words. Parts excepted are corrections of form and content by the supervisor.

Title of work (in block letters):

Towards high fidelity two-qubit gates with superconducting qubits

Authored by (in block letters):

For papers written by groups the names of all authors are required.

Name(s):	**First name(s):**
Heinsoo	Johannes

With my signature I confirm that

- I have committed none of the forms of plagiarism described in the 'Citation etiquette' information sheet.
- I have documented all methods, data and processes truthfully.
- I have not manipulated any data.
- I have mentioned all persons who were significant facilitators of the work.

I am aware that the work may be screened electronically for plagiarism.

Place, date	**Signature(s)**
04.07.14	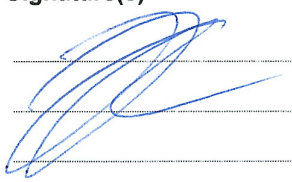

For papers written by groups the names of all authors are required. Their signatures collectively guarantee the entire content of the written paper.